J. Fluid Mech. (1995), *vol.* 290, *pp.* 225–262

An experimental study of a three-dimensional pressure-driven turbulent boundary layer

By SEMİH M. ÖLÇMEN AND ROGER L. SIMPSON

Aerospace and Ocean Engineering Department, Virginia Polytechnic Institute and State University, Blacksburg, VA 24061, USA

(Received 16 July 1993 and in revised form 7 December 1994)

A three-dimensional, pressure-driven turbulent boundary layer created by an idealized wing–body junction flow was studied experimentally. The data presented include time-mean static pressure and directly measured skin-friction magnitude on the wall. The mean velocity and all Reynolds stresses from a three-velocity-component fibre-optic laser-Doppler anemometer are presented at several stations along a line determined by the mean velocity vector component parallel to the wall in the layer where the $\overline{u^2}$ kinematic normal stress is maximum (normal-stress coordinate system). This line was selected by intuitively reasoning that overlap of the near-wall flow and outer-region flow occurs at the location where $\overline{u^2}$ is maximum. Along this line the flow is subjected to a strong crossflow pressure gradient, which changes sign for the downstream stations. The shear-stress vector direction in the flow lags behind the flow gradient vector direction. The flow studied here differs from many other experimentally examined three-dimensional flows in that the mean flow variables depend on three spatial axes rather than two axes, such as flows in which the three-dimensionality of the flow has been generated either by a rotating cylinder or by a pressure gradient in one direction only throughout the flow.

The data show that the eddy viscosity of the flow is not isotropic. These and other selected data sets show that the ratio of spanwise to streamwise eddy viscosities in the wall-shear-stress coordinate system is less scattered and more constant (about 0.6) than in the local free-stream coordinate system or the normal stress coordinate system. For $y^+ > 50$ and $y/\delta < 0.8$, the ratio of the magnitude of the kinematic shear stress $|\tau/\rho|$ to the kinematic normal stress $\overline{v^2}$ is approximately a constant for three-dimensional flow stations of both shear-driven and pressure-driven three-dimensional flows. In the same region, the ratio of the kinematic shear stresses $-\overline{vw}/-\overline{uw}$ appears to be a function of y^+ in wall-stress coordinates for three-dimensional pressure-driven flows.

1. Introduction

The present study is an experimental investigation of the characteristics of an incompressible three-dimensional turbulent boundary layer generated by a wing–body junction flow. As stated by Bradshaw (1987), the study of the effects of mean flow three-dimensionality on the turbulence structure still requires further reliable data sets which include all terms of the Reynolds stress tensor. Previous reviews of available three-dimensional turbulent boundary layer data have been made by several authors, including Johnston (1976), Fernholz & Vagt (1981), Anderson & Eaton (1987*a*), van den Berg (1987), and Schwarz & Bradshaw (1992). van den Berg pointed out three important characteristics of useful data sets: data reliability, sufficient data for comparisons with calculations, and data for flows representative of practical applications.

The test flow studied here is encountered in many flows of engineering interest, for example in the wing/body junction of an airplane and appendage/hull junctions on submarines. Previous wing/body junction studies of Shabaka & Bradshaw (1981) and McMahon, Hubbart & Kubendran (1982) dealt with constant-thickness wings with 6:1 and 3:2 elliptical noses, respectively. Shabaka & Bradshaw measured the double and triple velocity correlations at three different streamwise planes and the fluctuating velocity and mean velocities at eight streamwise planes. They studied the complete balances for the turbulent kinetic energy and momentum equations. McMahon *et al.* used horizontal and slanted hot wires supported on needles which projected into the boundary layer from the flat plate on which the wing was mounted. The study included all six Reynolds stresses in two streamwise planes. A 3:2 elliptical-nose NACA 0020 tail body, as used in the present study, was tested by Merati, McMahon & Yoo (1988) and by Dickinson (1986). In those studies Merati *et al.* used the same two hot-wire probes as used by McMahon *et al.* and measurements of all Reynolds stresses at five streamwise planes were made. Dickinson used X-configuration hot films and made measurements of all Reynolds stresses except $-\overline{vw}$ at seven streamwise planes. Fleming, Simpson & Devenport (1993) present single-wire hot-wire data near the wing studied here and compare their data with those of Merati *et al.* and Dickinson. Devenport & Simpson (1990*a*, *b*, 1992) present and discuss laser-Doppler anemometer data close to this wing. Those studies were directed primarily toward understanding the nature of the wing/body junction flow globally and investigating the horse-shoe vortex formed around the body and the wake flow. In all hot-wire anemometer studies, the prongs which hold the hot-wire and hot-film sensors produce interference with the flow when near the wall. For the flow away from the junction vortex, none of the studies mentioned above measured the near-wall structure with laser-Doppler velocimetry.

The 3:2 elliptical-nosed NACA-0020-tailed cylindrical wing studied here has a chord length of 30.5 cm (12 in.), maximum thickness of 7.17 cm (2.824 in.), and height of 22.9 cm (9.016 in.). The wing was mounted normal to a flat plate. The nominal reference velocity of the air is $U_{ref} = 27.5$ m s^{-1} and the momentum thickness Reynolds number Re_θ is 5940 at 0.75 chord upstream of the nose of the body on the centreline of the tunnel. The flow conditions are essentially the same as used by Devenport & Simpson (1990*a*) to examine the flow in the nose region of the same wing model. The reliability of the data here was confirmed by taking the velocity and stress measurements with two different techniques, laser-Doppler velocimetry and hot-wire anemometry. Skin-friction values are reported from an independent technique. The boundary conditions and the characteristics of the boundary layer approaching the wing were established at 0.75 chord upstream of the nose. Pressure data on the wall were taken at closely spaced locations.

The present study contains a unique data set which documents the flow characteristics along a path found by translating in the direction of the mean velocity vector component parallel to the floor at a point in the boundary layer where $\overline{u^2}$ is maximum. The maximum $\overline{u^2}$ location is in the near-wall region, a region where turbulent kinetic energy production is greatest. It is intuitively reasoned that the overlap of the near-wall flow and the outer-region flow in the boundary layer occurs at the location where the $\overline{u^2}$ is maximum.

The main goal here was to investigate flow features along the selected x, z path mentioned above, not a global characterization as in earlier studies. Such a path resembles the one studied by Dechow & Felsch (1977) in front of their cylinder/flat plate junction flow, although their path was along a free-stream streamline.

2. Experimental apparatus and techniques

The measurements were carried out in the Virginia Tech Aerospace and Ocean Engineering Department Low Speed Boundary Layer Tunnel, which has been used in previous work at Southern Methodist University and at Virginia Tech and is described by Devenport & Simpson (1990*a*). The inlet flow is tripped by the 0.63 cm blunt leading edge of the tunnel floor to ensure that the boundary layer is turbulent. The test section is 0.91 m wide and 8 m long. Inserts for the wind-tunnel sidewalls were used to minimize blockage-induced pressure gradients around the vertical wing.

A detailed study of the characteristics of the zero- and favourable-pressure-gradient mean two-dimensional boundary layer in this tunnel without the wing model can be found in Ahn (1986). His hot-wire data of u power spectra, mean flow, $u' = (\overline{u^2})^{1/2}$ and $v' = (\overline{v^2})^{1/2}$ fluctuating velocities, and $-\overline{uv}$ shear stress data showed good agreement with the measurements of previous researchers at comparable Reynolds numbers. At a nominal speed of 27.5 m s^{-1} the turbulence intensity observed in the tunnel free stream was 0.1 % and the potential core was uniform to within 0.5 % in the spanwise and 1 % in the vertical directions, respectively (Devenport & Simpson 1990*b*). The temperature was 25 °C ± 1.0 °C.

The blockage of the flow in the spanwise direction due to the tunnel sidewalls and inserts was negligible, as revealed by the computed and measured surface pressure distributions and oil-flow pictures discussed below. A gap of 37 mm was left between the model top and the tunnel roof to avoid the interaction of the roof boundary layer and the model, so as not to generate a second horse-shoe vortex which could interact with the studied flow on the tunnel floor.

A surface oil-flow technique was used to show the limiting streamline or skin-friction line structure. A self-adhesive black glossy plastic sheet was laid on the wall surface (Frisk Coverseal). The mixture used in this study was 20 ml of TiO_2, some kerosene so that that mixture was 55 ml, and finally 9 ml of oleic acid. It was observed that less TiO_2 resulted in lower contrast but clearer fine structure. Once the mixture was applied, the tunnel was operated until there was no visible movement of the mixture; then the plastic sheet was taken from the tunnel and further dried. A lacquer fixer was used to preserve the surface pattern and permit photocopying.

The wall skin-friction magnitudes used in this study were measured by Ailinger (1990) using the oil-flow skin-friction interferometry technique of Monson & Higuchi (1981); see also Monson (1984). The technique relates the thinning rate of an oil film applied on the surface to the skin friction at that point by using lubrication theory for thin films. The thinning rate of oil was measured with a laser interferometer and photodiodes. The film thickness was less than 100 μm when measurements were made, causing negligible interaction with the flow. The direction of the wall-shear stress is approximated by the LDV measured mean-flow angle nearest the wall.

The pressure measurements were made with a J-type Scanivalve and a conventional inclined manometer. The pressure tap holes were 1 mm in diameter. The pressure coefficient was calculated using

$$C_p = (p - p_{ref})/(p_0 - p_{ref}),$$

where p is the surface static pressure, p_0 and p_{ref} are the stagnation pressure and reference static pressure measured at the tunnel entrance. Values for p_0 and p_{ref} were obtained from a Pitot-static tube (United Sensor Probe, type PAC-8-KL) located 1.55 m downstream of the tunnel entrance.

The single hot-wire technique used in this study is described by Devenport & Simpson (1986). The technique is designed to measure U- and W-components of the mean velocity and $\overline{u^2}$, $\overline{w^2}$, $-\overline{uw}$ components of the Reynolds stress tensor with the assumption that V and $v' = (\overline{v^2})^{1/2}$ are small compared to the velocity magnitude in the (x, z)-, or (U, W)-plane, following the reasoning suggested by Jorgensen (1971). For the flow studied, this assumption restricts the use of the technique away from the wing–body junction vortex, as was done for all of the data here. A boundary-layer-type probe (TSI 1218T1.5) was used with a platinum-coated tungsten wire sensor 5 μm in diameter and 1.5 mm in length.

The constant-temperature-anemometer bridge used was designed by Miller (1976) and modified by Simpson, Heizer & Nasburg (1979). With an overheat ratio of 0.7, the linearized frequency response was flat up to 12 kHz. The calibrated and linearized output of the anemometer was fed into a universal waveform analyzer (DATA 6000, Data Precision Corporation, Analogic Corporation) which gathered 10^4 samples during 20 s to form a histogram.

In the current study a three-velocity-component fibre-optic LDV system was used, which is a sub-system of a five-velocity-component fibre-optic LDV system (Ölçmen & Simpson 1994*a*). The system can make five simultaneous velocity component measurements. It is designed for space–time measurements of the turbulence structure in three-dimensional turbulent boundary layers. The five-component system consists of two main sub-systems: an optical table and the probe head. The components on the optical table are lasers and the optical equipment necessary to generate and couple the laser beams into polarization-preserving single-mode fibres that terminate in the probe. Laser beams from the probe pass through a glass window in the wind tunnel floor and form three coincident probe volumes to measure three simultaneous orthogonal velocity components at the U, V, W measurement point and two separate probe volumes to measure separate V velocity components. The probe consists of three transmitting optics trains, each with its receiving optics train with a fibre to a photomultiplier (PM) tube that forms a unit that can be translated and adjusted independently of the other two units. All the components fit into a volume of 43 cm × 23 cm × 39 cm.

In the present study two lasers were used. Two beams (488 nm, blue, and 514.5 nm, green) from two lasers (INNOVA 90-5 for blue and INNOVA 90-6 for green with etalons) are used to generate the nine beams (four blue, and five green) to produce the five probe volumes. Out of these five probe volumes only three were used. The frequency of the laser beams was shifted to resolve the directional ambiguity. Frequency shifts for green beams are 0, −40, −50, +30 and −90 MHz and for the blue beams 0, 40, and −50 MHz. Final dimensions for the intersection of each of two beams are 60 μm diameter and 690 μm length. The included angles between the two couples of green beams used in the measurements are both 6.23° which result in a 4.73 μm fringe spacing. The included angle between the blue beams is 5.83° with a fringe spacing of 4.8 μm.

The light-scattering particles with an approximate diameter of 2 μm were generated from dioctal phthalate by an aerosol generator originally designed by Echols & Young (1963). The smoke was injected into the flow either through the air intake of the tunnel or at the entrance of the tunnel test section.

The PM tube voltage output signals which contain the Doppler frequency information were processed by three Macrodyne Frequency Domain Analyzers

(FDP 3100). A recent study comparing seven different processors with statistically prescribed waveforms shows that the frequency domain analyzers have less error in estimating the mean and r.m.s. quantities than counter processors (Hepner 1994). The analog signal from the PM tube was wide band-pass filtered to obtain clean signals rather than depending only on the processor band-pass filters. The measurements in the present study were made with signal validation ratios of at least 95% and mostly 98% to 100%, which resulted in minimal noise. The U, V, W velocities are measured in a coincidence mode with the FDPs. Owing to the lack of memory storage in the Macrodyne units, a computer board from Dostek (1400A Laser Velocimeter Interface with TCEM daughterboard option) and software were used in a 386/33C PC clone. With this board, data acquired from each of the three processors are accepted as valid data if all three data values occur within a time coincidence window (10 μs).

At every measurement point 30000 samples were acquired. The sampling rate varied from 50 samples/s very near the wall to 200 to 400 samples/s away from the wall. The U, V, W system data were systematically reduced in the following manner:

(*a*) The acquired Doppler frequencies were converted into velocities in the optical axes (a coordinate system defined by three directly measured orthogonal directions) and the histograms of these velocities were obtained. Also, the absolute arrival time for each velocity value was recorded.

(*b*) A parabola was fit to each side of the logarithm of the histogram ordinate in the range between 1% and 80% of the peak value. The data lying outside the intersection of the parabolas with the ordinate value of one occurrence of a velocity signal were discarded. For noisier histograms the edges of the histograms were interactively located and the data lying outside the skirts were again discarded. This type of reduction was necessary only for $y^+ < 8$ ($y^+ = u_\tau y/\nu$, $u_\tau = (\tau_w/\rho)^{1/2}$, where τ_w is the wall shear stress, ρ the density, and ν the kinematic viscosity) very near the wall. The clean velocity information was transformed into tunnel coordinates and saved.

(*c*) The velocity data in tunnel coordinates were once more cleaned using the parabola fitting and data discard routine of (*b*).

(*d*) The time-dependent clean velocity data in tunnel coordinates were then used to calculate the flow variables after accounting for velocity bias by a weighing factor inversely proportional to the instantaneous velocity magnitude (Fuchs, Nobach & Tropea 1994). Velocity component histograms over 512 bins ranging from the minimum to maximum value were calculated using this weighting factor. The mean value of these histograms results in mean velocities. Next the mean velocities were subtracted from the time-dependent data to obtain the time-dependent fluctuating velocities. Histograms using the weighting factor were calculated for all second- and third-order cross-products of the fluctuating velocities, and the mean values of these histograms resulted in Reynolds stresses and triple correlations.

Step (*a*) was important since the noise in the histograms calculated in optics axes was not necessarily in the skirts of the histograms in tunnel coordinates. In fact, for noisy histograms (noise above 5% of the peak value of the histogram) in optics axes, the calculated values in tunnel coordinates resulted in highly fluctuating data. At earlier stages of the study this type of data was observed.

Velocity components measured by the LDV system are subject to the velocity gradients within the probe volume of measurements. Gradient broadening corrections were rederived for the present beam system to correct the data (Ölçmen & Simpson 1994*b*). The effect of the gradient broadening was largest for the $\overline{u^2}$ and $-\overline{uw}$ stresses below $y^+ = 30$, being more significant closer to the wall in reduction of the values. The data presented here are not corrected for the gradient broadening. However, the

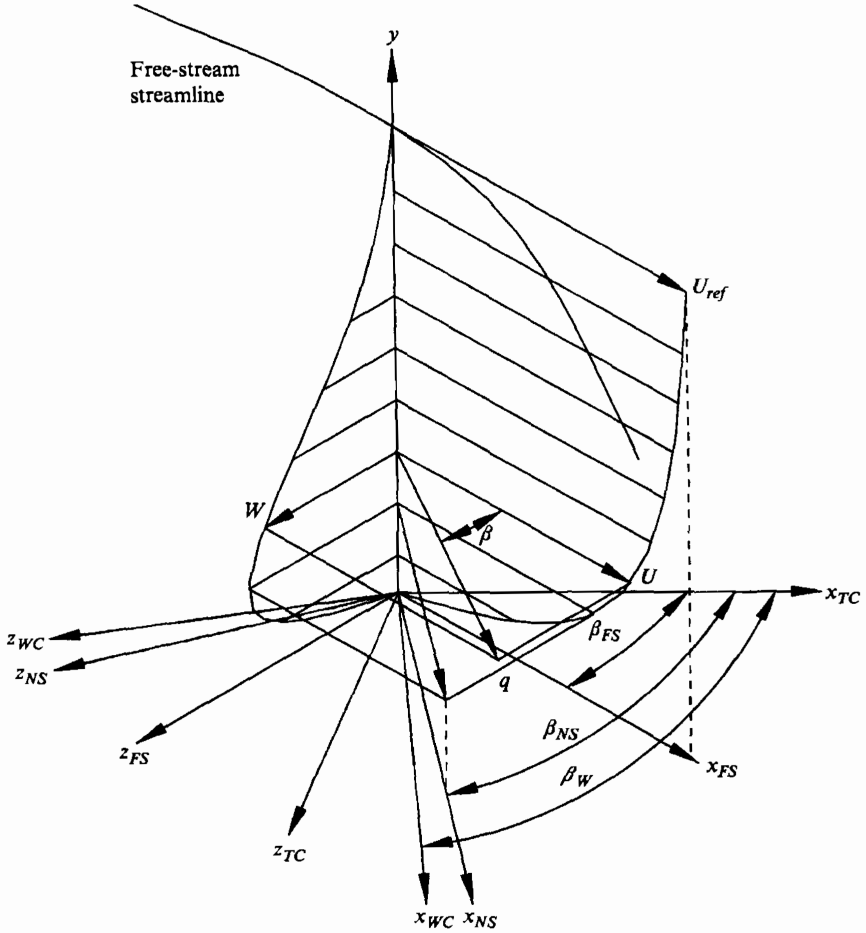

FIGURE 1. Definition of the angles and the right-handed coordinate axes used in the present study: x_{TC}, y_{TC}, z_{TC} = tunnel coordinates; x_{FS}, y_{FS}, z_{FS} = free stream coordinates; x_{NS}, y_{NS}, z_{NS} = maximum normal-stress coordinates; x_{WC}, y_{WC}, z_{WC} = wall-stress coordinates.

gradient broadening calculations showed that the effective coincident measurement probe volume of the U, V, W system is approximately 30 μm in diameter.

3. Description of coordinate systems and measurement locations

Figure 1 shows four sets of right-handed coordinate axes. In tunnel coordinates (TC) the x-axis is parallel to the tunnel centreline pointing downstream and the y-axis is perpendicular to the tunnel floor. For all coordinate systems used here, the y-axis was identically defined. In the local free-stream coordinate system (FS), the positive x-axis is in the direction of the mean velocity at the boundary layer edge, parallel to the tunnel floor. Subscript NS denotes the coordinate system of the maximum $\overline{u^2}$ normal-stress direction location. It is defined such that the positive x-axis is in the direction of the local mean velocity vector component which is parallel to the tunnel floor at the y-location where the normal stress $\overline{u^2}$ is maximum. Subscript WC stands for the wall-stress coordinate system. In this coordinate system, the x-axis is in the direction of the shear-stress vector at the wall approximated by the measured mean-flow angle closest

Station number	X (in.)	Z (in.)	U_{ref} (m s^{-1})	β_{FS} (deg.)	β_{NS} (deg.)
18	−9.48	1.08	27.4	1.2	0
17	−6.48	1.13	27.5	−0.7	1
16	−4.49	1.32	27.5	1.7	6.1
15	−3.50	1.45	27.5	2.2	8.5
14	−2.76	1.59	27.5	2.1	11.7
13	−2.29	1.75	27.5	5.5	21.5
12	−1.80	1.88	27.5	6.5	14.8
11	−1.33	2.04	27.5	9.0	18
10	−0.90	2.33	27.5	11.0	32.1
9	−0.47	2.58	27.4	12.1	30.2
8	0.19	2.72	27.4	13.9	30.9
7	0.26	2.94	27.5	10.5	25.3
6	0.73	3.12	27.5	9.5	20.8
5	1.19	3.30	27.6	9.2	20.8
4	1.67	3.43	27.5	7.3	15.9
3	2.17	3.53	27.5	5.0	10.9
2	2.66	3.6	27.5	5.0	8.4
1	3.66	3.68	27.6	4.3	4.5

TABLE 1. Left-hand-side hot-wire locations

Station number	X (in.)	Z (in.)	U_{ref} (m s^{-1})	β_{FS} (deg.)	β_{NS} (deg.)
1	−3.50	−1.45	27.0	−3.1	−8.5
2	−2.29	−1.75	27.0	−3.9	−21.5
3	−1.33	−2.04	27.0	−6.8	−18.0
4	−0.47	−2.58	27.0	−9.3	−30.2
6	1.19	3.30	27.0	−5.4	−20.8
7	−2.17	−3.53	27.1	−4.6	−10.9

TABLE 2. Right-hand-side hot-wire locations

to the wall, the y-axis is perpendicular to the wall and the z-axis completes a right-handed coordinate system.

The measurement locations can be seen in figures 2 and 3. The measurements performed in this study include single hot-wire (HW) measurements at 39 locations and laser-Doppler velocimeter (LDV) measurements at seven locations. An objective of these measurements was to observe how the flow characteristics changed in a three-dimensional pressure-driven boundary layer flow along a line whose x, z direction is given by the U, W velocities where the $\overline{u^2}$ normal stress is maximum. Hot-wire measurements were made to find this line and to compare with the LDV measurements, besides revealing some other flow quantities. They were obtained at 18 locations on the left side of the model (table 1) and at seven locations on the right-hand side at the LDV locations (table 2). The location of the most downstream profile was chosen to be away from the near-wing horse-shoe vortex as observed from the surface oil-flow visualization (figures 2*a*, *b*). This location was also chosen such that the governing equations of the hot-wire reduction programs would not be violated, but yet the effect of spanwise pressure gradients on the flow three-dimensionality would be as large as possible. The next 17 upstream points were found by finding the direction of the

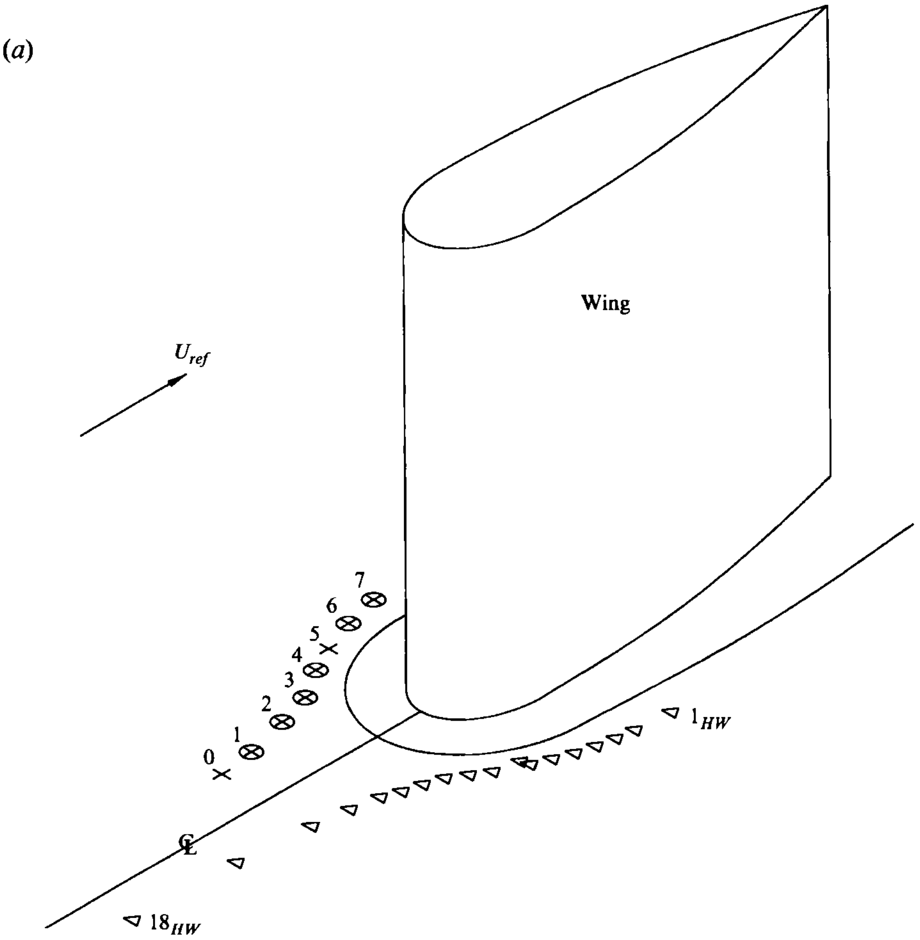

FIGURE 2(*a*). For caption see facing page.

maximum-normal-stress y-location obtained in each profile and translating 0.5 in. in the direction of the mean velocity component parallel to the wall at that location. At some locations near the leading edge or ahead of the body where the effect of three-dimensionality was weaker, the distance translated was greater than 0.5 in. Another 12 hot-wire profiles were taken 0.75 chord upstream of the body on a crosswise line to define the inlet boundary conditions of the flow (table 3). The flow 0.8 chord length ahead of the body, as seen from the hot-wire measurements made at the most upstream eighteenth hot-wire station on the left-hand side, was again two-dimensional since the W-component of the mean velocity component and the $-\overline{uw}$ shear stress component were near zero. Therefore, the flow upstream can be assumed to be a closely two-dimensional turbulent boundary layer. Locations of the hot-wire profiles at 0.75 chord upstream of the wing, boundary layer thicknesses, displacement and momentum thicknesses calculated with the trapezoidal rule, skin-friction coefficients computed using the two-dimensional law of the wall (Kármán constant of 0.41 and additive constant of 5.0) and six point line fit to the semi-logarithmic regions of the U/U_{ref} profiles are tabulated in table 3.

The LDV experimental data include the mean velocities and all six components of the Reynolds stress tensor. The LDV measurements were made on the right-hand side

(b)

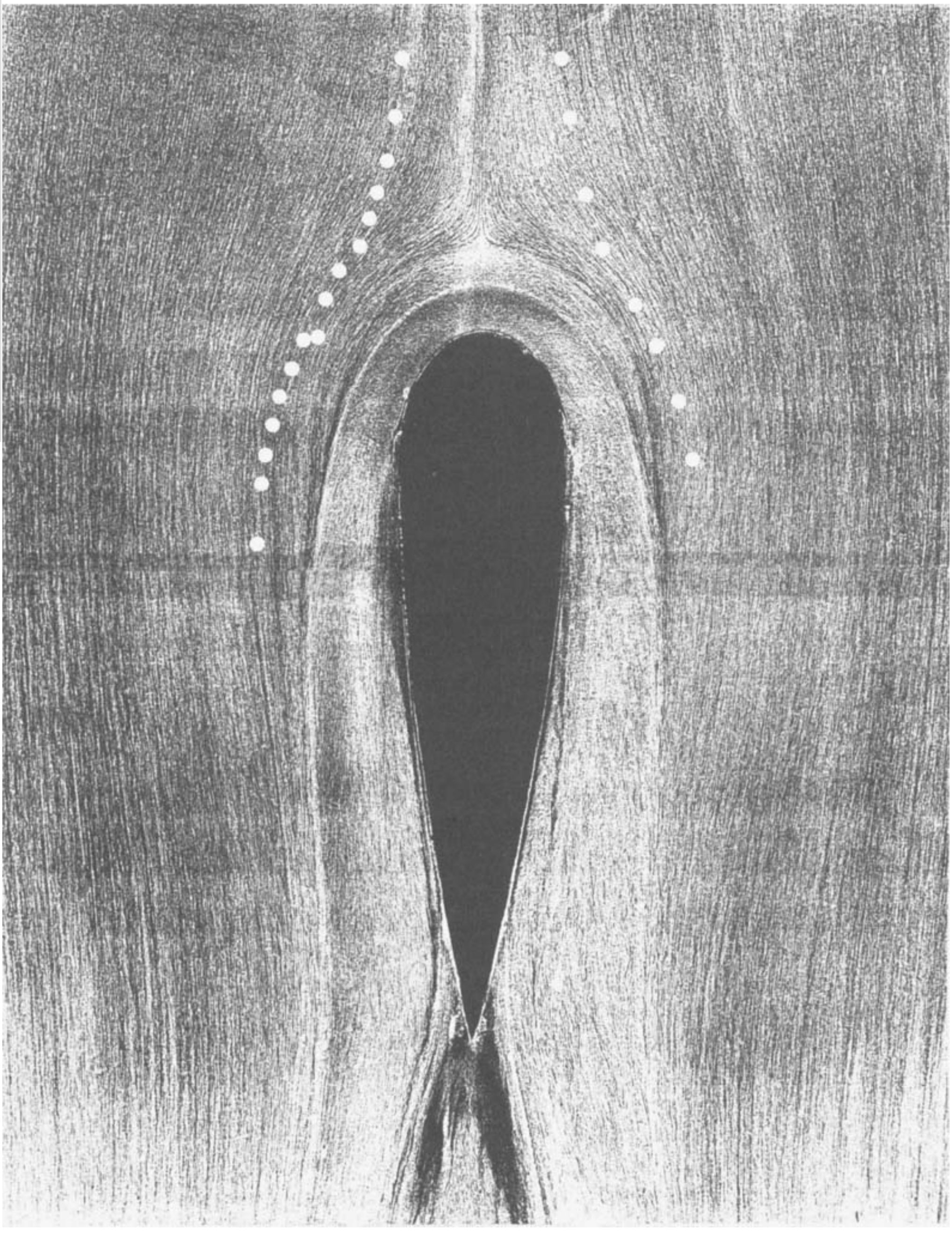

FIGURE 2. (a) Schematic of the wing–body junction and the velocity and stress measurement locations. Numbers 0–7 denote right-hand-side hot-wire and laser-Doppler velocimeter measurement locations. Numbers 1–18 denote left-hand-side hot-wire measurement locations. (b) Oil flow visualization on the test wall surrounding the wing at 27.5 m s^{-1} nominal reference velocity. The white dots on both sides denote the velocity and stress measurement locations.

Z_{TC}/t	U_{ref}	$C_f \times 10^3$	δ_1 (mm) displacement thickness	δ_3 (mm) momentum thickness	$H = \delta_1/\delta_3$
0	27.3	3.06	4.68	3.34	1.40
0.25	27.3	2.68	4.68	3.43	1.37
0.5	27.3	3.07	4.75	3.43	1.39
0.75	27.3	2.76	4.68	3.51	1.33
1.0	27.3	3.03	4.70	3.44	1.37
1.25	27.3	3.05	4.75	3.50	1.36
1.5	27.2	2.92	4.66	3.45	1.35
1.75	27.3	3.30	4.78	3.53	1.35
2.0	27.3	3.0	4.65	3.49	1.33
2.25	27.0	2.68	4.78	3.55	1.35
2.5	27.1	2.74	4.79	3.41	1.40
2.75	27.0	3.54	4.83	3.57	1.35
3.25	26.9	3.03	4.88	3.47	1.41
3.75	26.9	3.09	4.74	3.56	1.33
4.25	26.9	3.06	4.78	3.53	1.35

TABLE 3. 0.75 chord upstream hot-wire profile locations

of the body at the symmetric locations of the previous hot-wire points but only at seven points (table 4). To check the symmetry of the flow before LDV measurements were made, seven more hot-wire profiles were taken (table 2). The data gathered from pressure measurements, surface oil-flow visualization patterns and these hot-wire measurements show that the flow around the body is symmetric.

4. Experimental results

4.1. *Oil-flow visualization results*

The structure of the limiting-streamline surface skin-friction line of the flow field ahead and around the body is shown in figure 2(*b*) to be symmetric about the wing chord. The separation line, which forms due to the adverse pressure gradient and passes through the saddlepoint, and the line of low shear (open separation) where the mixture accumulates due to the lower skin friction, are shown upstream and around the side of the model. The fishtail-shaped wake flow limiting-streamline characteristics and the near trailing edge separation of the flow on the wing very close to the floor are also clearly observable. The same flow characteristics were also observed by Dickinson (1986) in his study of a wing–body junction flow using the same wing shape as in the present study.

4.2. *Pressure measurement results*

The measured static pressure distributions on the flat plate surface are plotted on the upper half of figure 3. Positive C_p values correspond to slower free-stream flow regions while the negative C_p values show regions faster than the reference velocity. Along the centreline the flow decelerates towards a stagnation point on the leading edge ($C_p = +1$).

The measured pressure values on both sides of the model, on the model, and 9 in. ($z/t = 3.187$) away from it at several x/t locations also show the symmetry of the flow. The measurements at these locations were compared with results from a two-dimensional potential-flow code for an infinite wing, which was selected to have 100 source and sink panels for each side of the model. The source density distribution code

Station	X (in.)	Z (in.)	U_{ref} (m s^{-1})	U_e (m s^{-1})	β_{FS} (deg.)	β_w (deg.)	β_{NS} (deg.)	u_τ (m s^{-1})	ν (m^2 s^{-1}) ($\times 10^5$)	$(\partial C_p/\partial x)_{FS}$ (m^{-1})	$(\partial C_p/\partial z)_{FS}$ (m^{-1})	Daily pressure (millibar)	Daily temperature (°C)
0	−4.49	−1.32	27.6	26.4	−1.68	−6.1	−4.88	0.87	1.68	0.778	0.916	938	25.4
1	−3.50	−1.45	27.5	24.9	−2.64	−11.5	−8.5	0.864	1.65	1.2	1.39	949	24.6
2	−2.29	−1.75	27.5	24.8	−4.81	−24.0	−21.5	0.865	1.65	0.204	2.99	949	24.3
3	−1.33	−2.04	27.5	25.3	−8.63	−33.7	−18	0.957	1.65	−3.91	4.07	947	23.5
4	−0.47	−2.58	27.5	27.3	−9.45	−30.6	−30.2	1.11	1.65	−6.34	0.923	946	24
5	0.26	−2.94	27.5	29.5	7.71	−19.7	−25.3	1.15	1.67	−6.25	−1.95	940	24.5
6	1.19	−3.30	27.5	30.5	−5.09	−7.17	20.8	1.16	1.68	−4.06	−5.53	934	25
7	2.17	−3.53	27.5	31.0	−2.71	−3.50	−10.9	1.20	1.68	0.26	−6.69	934	24.7

TABLE 4. Laser-Doppler velocimeter locations and flow parameters. Station 0 data from Ölçmen (1990). Pressure coefficient gradients are calculated from the measured distribution. U_e = Velocity magnitude at the layer edge.

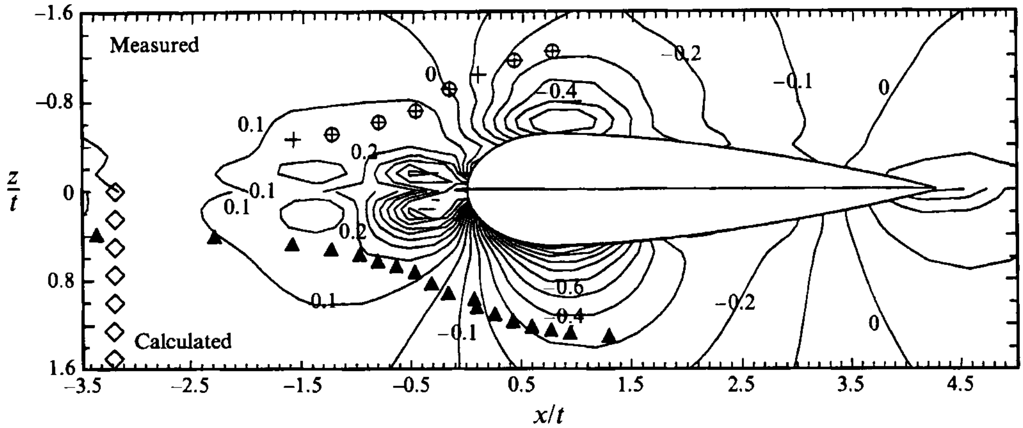

Figure 3. Contours of measured and calculated mean static pressure coefficients (C_p) on the test wall (two-dimensional inviscid calculation of Ölçmen 1990); ▲, left-hand-side hot-wire; ○, right-hand-side hot-wire; +, LDV; ◇, hot-wire measurement locations 0.75 chord upstream of wing nose.

was written using the formulation presented by Bertin & Smith (1979). The C_p contour plots of the potential-flow results and the data show differences (figure 3). On and near the body these may be attributed to the horse-shoe vortex and to the separation of the flow on the model before the trailing edge, but not to tunnel blockage effects.

The streamwise pressure gradients at $z/t = 0.5$ are positive until $x/t = -0.5$; downstream, high negative gradients are present until $x/t = 0.756$, after which lower positive gradients start. The magnitude of the gradients away from the body are lower than the near-body values. C_p values on the flat plate show a gradual increase, with a peak at the leading edge when the flow approaches the wing. At the sides of the wing, the flow accelerates, resulting in C_p values below zero. After $x/t = 3.25$, C_p values again increase at both sides of the wing when the flow decelerates. Measured pressure gradients at the LDV measurement stations are tabulated in table 4.

The lateral pressure gradients ahead of the wing at $x/t = -2$ are close to zero. The acceleration of the flow around the nose of the wing results in the sharp drop in C_p and high lateral pressure gradients between $x/t = 0.25$ and 0.75. In the aft region of the airfoil, but upstream of $x/t = 3.25$, the pressure gradients are milder. After this point the gradient changes sign.

4.3. *Velocity and stress measurements*

The LDV velocity and stress data are presented in local free-stream coordinates. The flow structure observed in other coordinate systems and the hot-wire data will be included when they are relevant. The free-stream direction was found separately for each profile, by taking the last point in each profile. The transformations from tunnel coordinates to the free-stream coordinates, normal-stress coordinates, or the wall-stress coordinates were done by using the same angles throughout each profile and a tensor transformation (Frederick & Chang 1972). In the transformation to normal-stress coordinates, angles obtained with the hot-wire technique were used, while for wall-stress coordinates the mean flow angles from LDV measurements at the first point of the profiles near the wall were used.

Hot-wire measurements were made on both sides of the wing. Right-hand-side hot-wire measurements were done at the same locations as the laser measurements. The comparison of these six profiles with the left-hand-side profiles of the corresponding location showed that the mean and turbulence quantities agreed well, which in turn showed that the flow is symmetric (Ölçmen 1990). The uncertainty in probe y-location at the first point of the profiles was ± 0.003 in.

After measurements with the hot-wire system and the LDV technique were completed, it was observed that u' from these two measurement techniques did not match in the inner layer and in the semi-logarithmic region of the profiles. The differences between the u' fluctuating velocity component measured with the hot-wire and LDV techniques near the wall and in the regions corresponding to the semi-logarithmic regions of the U/U_{ref} profiles are on the order of 10%. The source of the discrepancy could not be located even after re-examination of all equipment and the mean velocity gradient broadening correction of George & Lumley (1973) for the LDV data with rederived equations for the current system (Ölçmen & Simpson 1994*b*). This effect may be due to the fairly large aspect ratio (length of wire/diameter of wire = 300) of the wire as shown by Ligrani & Bradshaw (1987). Hot-wire measurements were not corrected.

Gradient-broadening-corrected LDV data are shown separately in the figures. Estimated uncertainties at 20:1 odds are given below for each discussed quantity. To confirm the uncertainties and the repeatability of the measurements at station 5, data were retaken on a separate day. Fluctuating velocity, shear stresses, and derived quantities are presented for stations 1–7.

4.3.1. *Mean flow measurement results*

Mean velocity profiles of U/U_{ref} *vs.* (y/δ) are plotted in figure 4(*a*), where δ is the boundary layer thickness where $U/U_e = 0.995$ at each station and U_{ref} is the reference velocity (tables 4 and 5) at the tunnel test section entrance. The U/U_{ref} profiles obtained with the hot-wire and LDV techniques showed good agreement with an uncertainty of about ± 0.003.

The deceleration of the flow up to station 2 is followed by an accelerating flow region. The semi-logarithmic region in the profiles is clearly observed. The slope of this region with respect to the slope of the first station shows little change at the second location and continuously decreases till the sixth station. At the seventh location a slight increase with respect to the sixth station is observed.

The scale for the V/U_{ref} data (± 0.001 uncertainty) shown in figure 4(*b*) is close to 1/25 of that for U/U_{ref}. The magnitude of the maximum at the first three stations shows a gradual decrease, but starting with the fourth station profile, the maximum increases. At these last four stations, the maximum is approximately at 11–16 mm away from the wall. In all the profiles, the magnitude near the boundary layer edge decreases. This results in the hill-shaped profiles characteristic of the last five stations. Overall, the maximum V-component measured was $\approx 0.025 U_{ref}$, which is two orders of magnitude smaller than the U-component. This in turn shows that neglecting the V-component in the hot-wire reduction equations is acceptable (also, $v'/U_{ref} \approx 0.05$ at maximum).

Profiles of W/U_{ref} (± 0.002 uncertain) from LDV data are shown in figure 4(*c*). Starting with the second station location, the semi-logarithmic regions begin only at the end of the semi-logarithmic regions for the U-velocity and span into the outer regions. The profile absolute maximum values increase until the fourth station is reached. The fourth and fifth station profiles closely resemble each other; sixth and seventh station profiles show a decrease in the maximum velocity observed. It is also clearly observable that the maxima of the profiles shift to a higher y-location at each successive location.

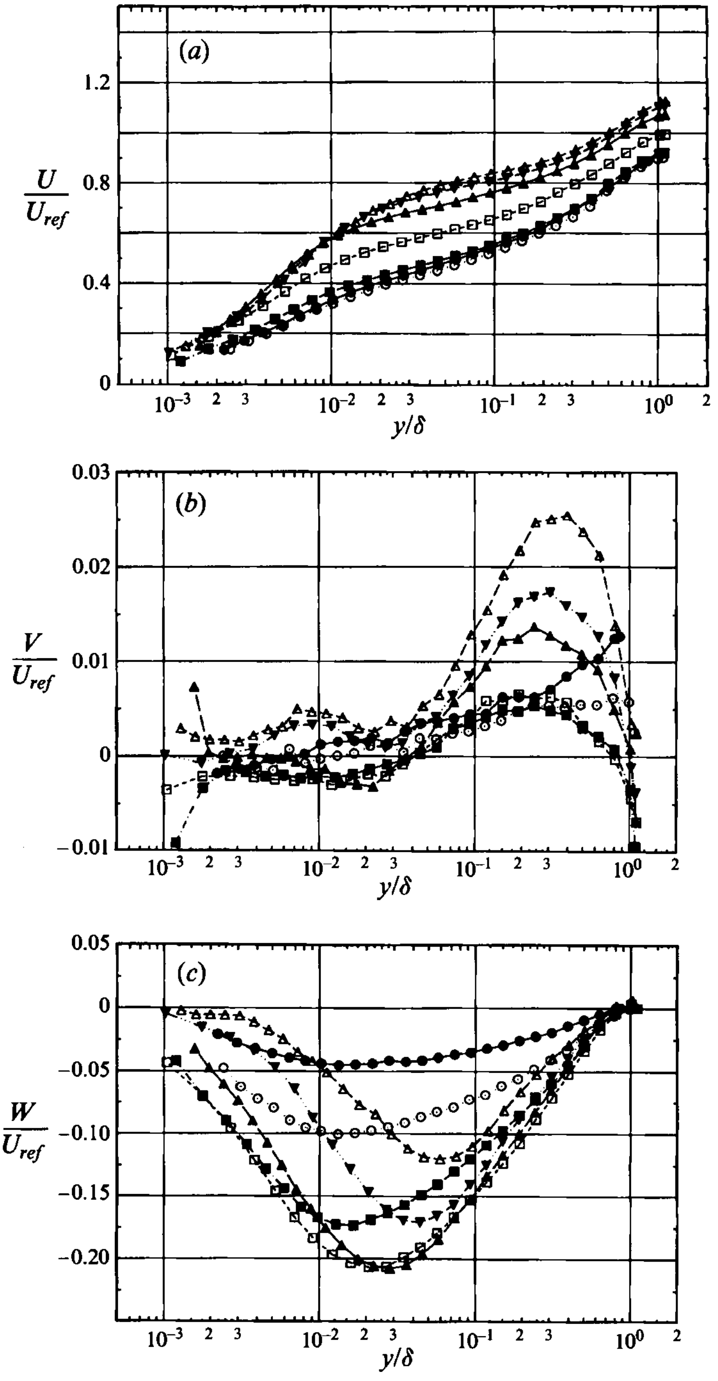

FIGURE 4. (a) U-component of the mean velocity vector measured with LDV technique presented in free-stream coordinates. (b) V-component of the mean velocity vector measured with LDV technique for all four coordinate systems of figure 1. (c) W-component of the mean velocity vector measured with LDV technique presented in free-stream coordinates. Stations: ●, 1; ○, 2; ■, 3; □, 4; ▲, 5; ▼, 6; △, 7. The uncertainties are on the order of the symbol size.

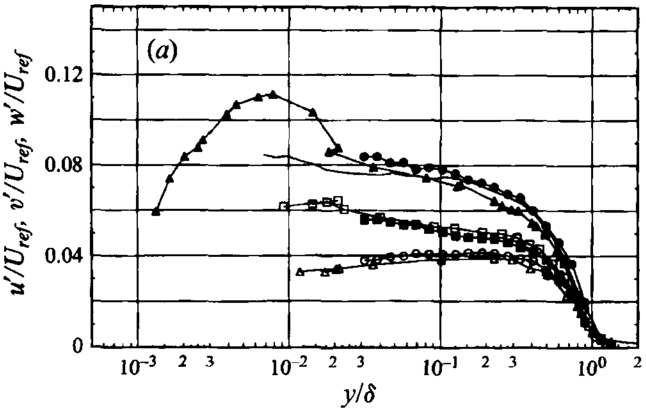

FIGURE 5(*a*). For caption see page 241.

4.3.2. *Fluctuation velocity results*

For station 0, figure 5(*a*) shows the LDV data, the hot-wire data for u' obtained at the left-hand-side symmetrical location, and Klebanoff's (1955) hot-wire data for a two-dimensional flow with Re_θ close to that of the flow here (Ölçmen 1990). The flow at this station is almost two-dimensional with an imposed adverse pressure gradient. Figure 5(*a*) shows that the v' and w' fluctuating velocities are in good agreement and that the u' fluctuating velocities obtained with hot-wire, Klebanoff's data, and the LDV data are in fair agreement. The differences between data from the two hot-wire techniques very near the wall are believed to be due to the large-aspect-ratio wire, as discussed previously in §4.3.

In the first three profiles, below $y/\delta = 0.03$ ($y^+ \approx 65$), u'/U_{ref} decreases approximately 0.005 as the flow moves downstream (figure 5*b*). The uncertainty is ± 0.001. Starting with the fourth station, and proceeding downstream, u'/U_{ref} in this region increases above the values observed at the first station, especially very near the wall. An increase of 0.03 of the maximum is observed at station 7 with respect to station 4. In the outer region, u'/U_{ref} continuously decreases downstream of station 3 by about 0.0125. This suggests that the effect of three-dimensionality is different in different regions of the flow. Above $y/\delta \approx 0.03$ or 0.04 ($y^+ \approx 65$ or 110), the flow is relaxing; below this region the u'/U_{ref} seems to be affected by the near-wall three-dimensional effects.

The v'/U_{ref} profiles seem to be similar to each other with an uncertainty of ± 0.0009 except nearest the wall. An increase of the fluctuations on the order of 0.005 to 0.01 occurs from the first to fourth station within the whole layer. At the last two stations, a levelling off of the fluctuations between $y/\delta \approx 0.025$ and 0.07 ($y^+ \approx 70$ and 180) occurs while the fluctuations between $y/\delta \approx 0.01$ and 0.02 ($y^+ \approx 25$ and 55) and 0.1 and 0.4 continue to increase. At the last three stations below $y/\delta \approx 0.005$ ($y^+ \approx 15$) there is a decrease on the order of 0.01 with respect to station 4 values. Nearest the wall the uncertainties are higher since v' must vary as y^2.

Proceeding in a downstream direction the w'/U_{ref} profiles show an increase below $y/\delta \approx 0.2$ ($y^+ \approx 550$) on the order of 0.01 till station 6. The uncertainty is ± 0.0008. At the last station a slight decrease is observed. Above this height w'/U_{ref} decreases and is similar in each profile.

While u' increases to peak values close to the wall, v' increases gradually to more like a plateau around $y/\delta \approx 0.02$ to 0.04 ($y^+ \approx 60$ to 150) and w' reaches a peak or a plateau

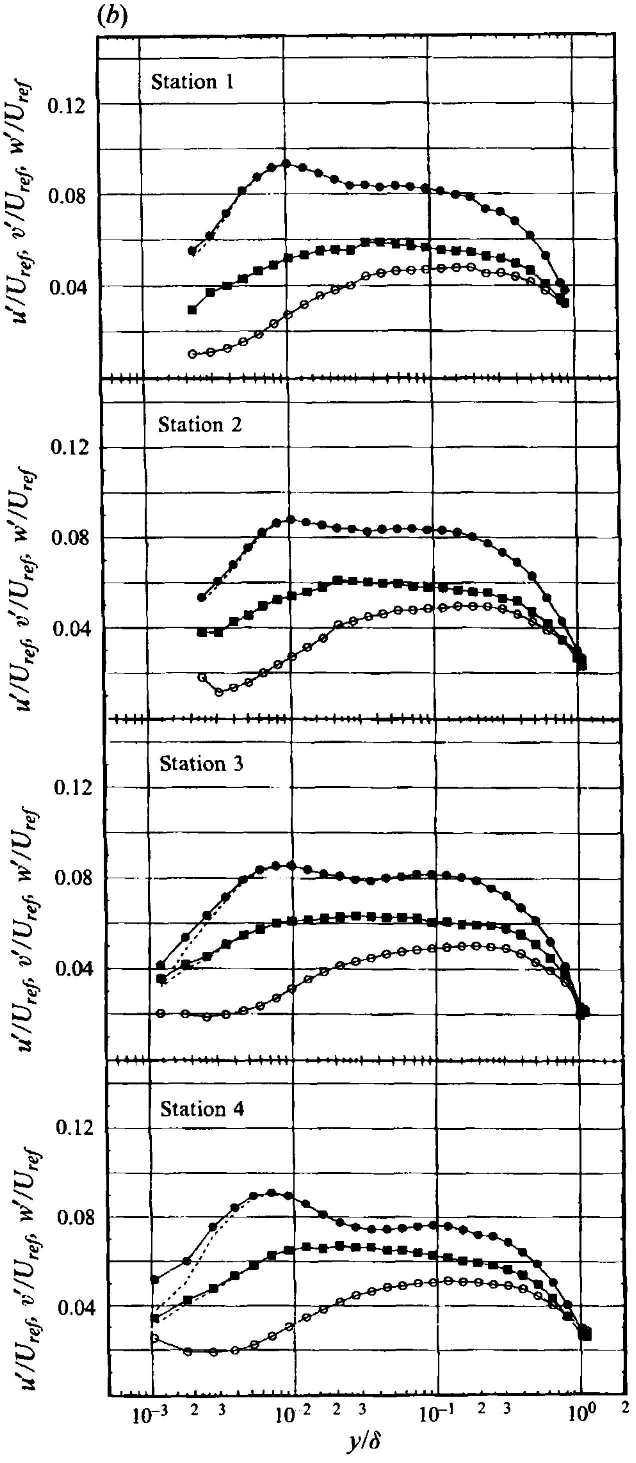

FIGURE 5(*b*). For caption see facing page.

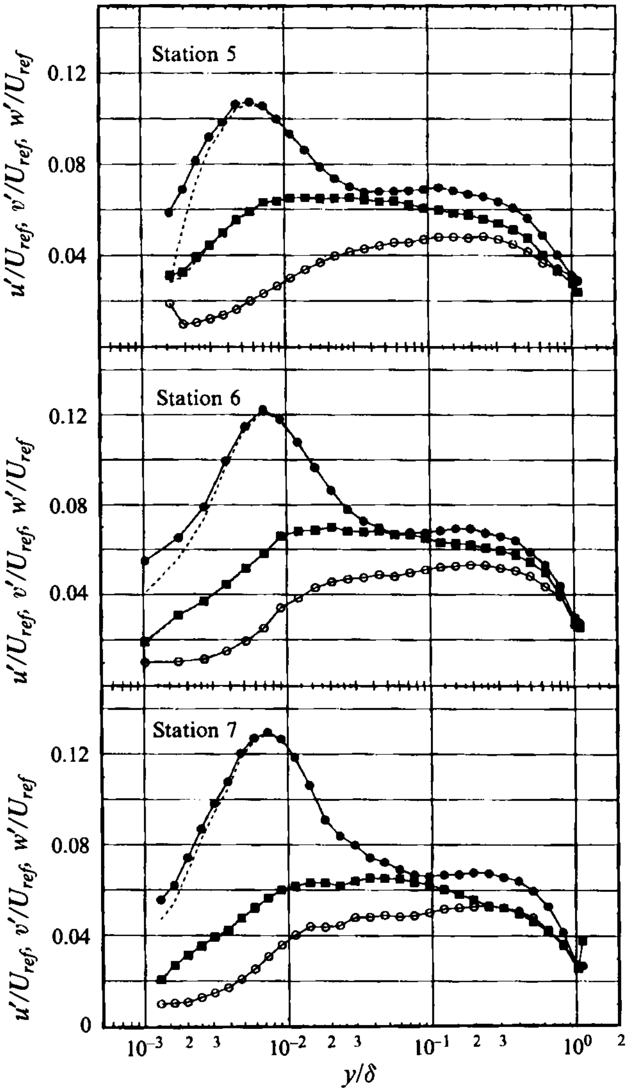

FIGURE 5. u'/U_{ref}, v'/U_{ref} and w'/U_{ref} fluctuating velocity components measured with the LDV technique presented in local free-stream coordinates. (*a*) Station zero: ●, u'; ○, v'; ■, w'; ▲, △, □, u', v' and w' data of Klebanoff (1955) respectively; —, 16th left-hand-side hot-wire data. (*b*) Stations1 – 7: ●, u', ○, v'; ■, w'. Dashed lines denote gradient-broadening-corrected data The uncertainties are on the order of the symbol size.

closer to the wall than v'. Note that at the last three stations, u' and w' are nearly equal at one position in the profiles. The u' and v' profiles form a plateau region where stresses are nearly constant. The length of the region changes with each station.

4.3.3. *Reynolds shear stress results*

At the first station where the flow is almost two-dimensional, $-\overline{uv}/U_{ref}^2$ stresses rapidly increase to a value of 0.0012 away from the wall (figure 6). The uncertainty is ± 0.00008. Near the wall below $y/\delta \approx 0.03$ ($y^+ \approx 65$) there is a reduction in the stress value; however, there is a gradual increase above this height till $y/\delta \approx 0.4$ including station 3. Downstream of this station while the value of the stress at $y/\delta \approx 0.03$ ($y^+ \approx$

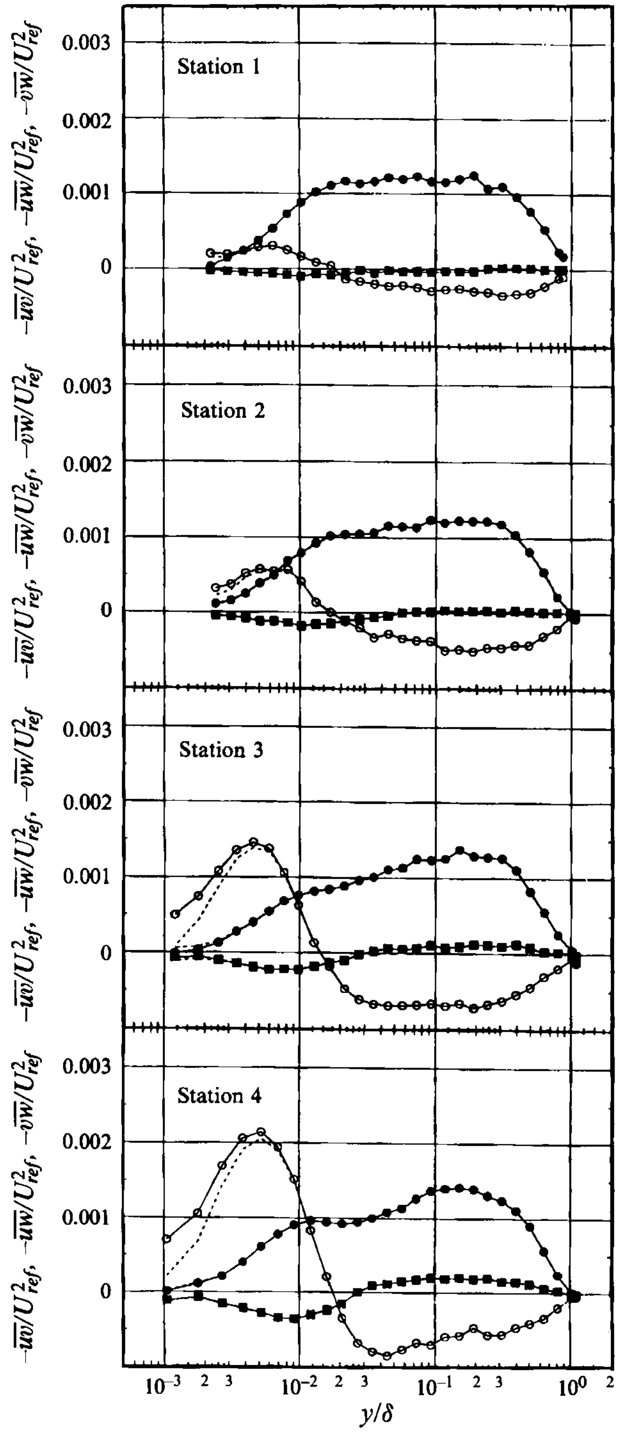

FIGURE 6. For caption see facing page.

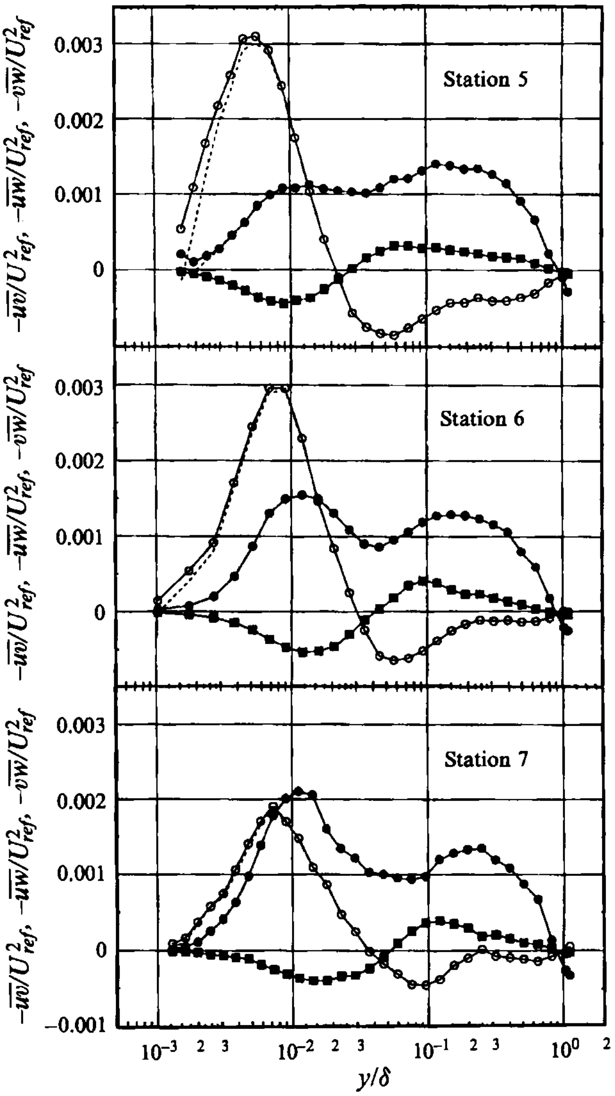

FIGURE 6. $-\overline{uv}/U^2_{ref}$, $-\overline{uw}/U^2_{ref}$ and $-\overline{vw}/U^2_{ref}$ kinematic shear stress components measured with the LDV technique presented in free-stream coordinates for stations 1–7: ●, $-\overline{uv}$; ○, $-\overline{uw}$; ■, $-\overline{vw}$. Dashed lines denote gradient-broadening-corrected data. The uncertainties are on the order of the symbol size.

65) stays constant at locations below and above this height, there is an increase in the stress resulting in double-peaked profiles. The maximum at station 7 is close to twice the maximum at station 1.

The $-\overline{vw}/U^2_{ref}$ stresses at the first station are close to zero. The uncertainty is ± 0.00002. With the effect of three dimensionality, $-\overline{vw}/U^2_{ref}$ stresses gradually increase to values around ± 0.0005 both below and above $y/\delta \approx 0.03$ to 0.05 ($y^+ \approx 80$ to 150) where the stress changes its sign. Near-wall values are close to zero. Proceeding downstream, the location where the stress changes its sign occurs at a higher location. At station 7 an overall decrease in the values with respect to station 6 values are also observed.

The $-\overline{uw}/U_{ref}^2$ stress starts developing at the first station. The uncertainty is about ± 0.00004. Near the wall the stress changes sign. This location is at a progressively greater y proceeding downstream and is located between $y/\delta \approx 0.015$ and 0.03 ($y^+ \approx 50$ and 100). This stress gradually increases in magnitude proceeding downstream; at station 6 the peak value of 0.0032 obtained at $y/\delta \approx 0.0055$ ($y^+ \approx 20$) is approximately twice the average magnitude of the $-\overline{uv}$ stress at the same station. At station 7 there is a decrease in the peak value. The magnitude of the stress in the negative side increases till the fifth station and decreases at downstream locations.

5. Examination of the Reynolds-averaged flow structure

Some derived quantities of interest for Reynolds-averaged modelling can be computed from these results. The quantities discussed here are the following profiles: the flow angle, velocity gradient angle, and shear stress angle; the spanwise ϵ_z and the streamwise ϵ_x eddy viscosities and the eddy viscosity ratio or anisotropy factor N; the mixing length L_m; the specific turbulence kinetic energy $\text{TKE} = \frac{1}{2}(\overline{u^2}+\overline{v^2}+\overline{w^2})$; the ratio A_1 of shearing stress $|\tau| = [(-\rho\overline{uv})^2+(-\rho\overline{vw})^2]^{1/2}$ in a plane parallel to the wall to twice the TKE; stress ratios $\overline{v^2}|\tau/\rho|$ and $-\overline{vw}/-\overline{uw}$.

The boundary layer thickness, displacement thicknesses, and momentum thicknesses at each station were computed using the trapezoidal rule for the integrations. The definitions and the values for these lengths may be found in table 5. All the derived quantities are calculated from data in local free-stream coordinates unless otherwise denoted.

5.1. *Flow angle, flow gradient angle and shear stress angle*

The flow angle (FA) shows the degree of three-dimensionality of the flow. The shear stress angle (SSA) and the flow gradient angle (FGA) give the comparative directions of the shear stress vector and the velocity gradient vector in the (x, z)-plane. If the effective eddy viscosity is isotropic, these two vectors are in the same direction. The difference between FGA and SSA not only gives the anisotropy of the flow but also how the anisotropy develops with increasing three-dimensionality of the flow. The uncertainties in FA, FGA, and SSA are ±0.25°, ±1°, and ±2.6°, respectively.

The mean flow angle FA is calculated using

$$\text{FA} = \arctan(W/U).$$

At station 1, the flow angle changes almost semi-logarithmically away from the wall (figure 7). For all stations the flow angle varies semi-logarithmically, although at different regions in the layers. At stations 1, 2 and 3 the flow angle near the wall below $y^+ \approx 10$ ($y/\delta \approx 0.005$) is about constant, showing nearly collateral near-wall flow regions. At station 4 this region extends to $y^+ \approx 30$ ($y/\delta \approx 0.012$). The flow direction near the wall is further from the wing than the local free-stream direction. Starting with station 4 the maximum flow angle decreases and the flow angle decreases near the wall due to the change in the sign of the lateral pressure gradient. At stations 6 and 7 the near-wall flow angle is close to the free-stream angle.

The flow gradient angle (FGA) was computed using the computed velocity gradients and

$$\text{FGA} = \arctan(\partial W/\partial y / \partial U/\partial y).$$

The gradients in the y-direction were computed by fitting parabolas to the W- and U-velocity component profiles in free-stream coordinates at each successive five points in

Station	δ (mm)	δ_1 (mm)	δ_2 (mm)	δ_3 (mm)	δ_4 (mm)	δ_5 (mm)	δ_6 (mm)	δ_7 (mm)
0	38.6	6.43	6.43	4.56	0.08	−0.07	0.01	0.0
1	39.2	6.91	6.89	4.76	0.58	−0.19	0.39	−0.02
2	40.2	7.55	7.48	5.11	1.34	−0.44	0.91	−0.08
3	39.3	7.02	6.86	4.86	1.87	−0.62	1.24	−0.19
4	39.0	5.95	5.76	4.38	2.15	−0.60	1.54	−0.25
5	39.6	5.37	5.23	4.14	1.90	−0.47	1.43	−0.20
6	39.2	5.21	5.11	4.06	1.57	−0.36	1.21	−0.14
7	38.8	5.06	5.01	3.97	1.06	−0.25	0.82	−0.07

U_e = Velocity magnitude at the layer edge.
$\delta = y$ where $U/U_e = 0.995$ = boundary layer thickness;

$$\delta_1 = \int_0^\infty \left(1-\frac{U}{U_e}\right)\mathrm{d}y = \text{streamwise displacement thickness;}$$

$$\delta_2 = \int_0^\infty \left(1-\frac{(U^2+W^2)^{1/2}}{U_e}\right)\mathrm{d}y = \text{magnitude displacement thickness;}$$

$$\delta_3 = \int_0^\infty \left(1-\frac{U}{U_e}\right)\frac{U}{U_e}\mathrm{d}y = \text{streamwise momentum thickness;}$$

$$\delta_4 = \int_0^\infty \left(-\frac{W}{U_e}\right)\mathrm{d}y = \text{lateral displacement thickness;}$$

$$\delta_5 = \int_0^\infty \frac{W}{U_e}\left(1-\frac{U}{U_e}\right)\mathrm{d}y = \text{lateral momentum thickness;}$$

$$\delta_6 = \int_0^\infty \left(-\frac{WU}{U_e^2}\right)\mathrm{d}y = \text{cross-product momentum thickness;}$$

$$\delta_7 = \int_0^\infty \left(-\frac{W^2}{U_e^2}\right)\mathrm{d}y = \text{crossflow momentum thickness.}$$

TABLE 5. Some length scales obtained from LDV data in local free-stream coordinates. Station 0 data from Ölçmen (1990)

the profiles, and the derivatives were computed from the derivatives of the parabolas at the middle (third) point.

The shear stress angle (SSA) is the angle which the shear stress vector component in the (x,z)-plane makes with the x-coordinate and is computed using

$$\mathrm{SSA} = \arctan(-\overline{vw}/-\overline{uv}).$$

Including station 1, FGA near the wall is less than zero and in the outer layer is greater than zero. The y-location where FGA is zero is at increasingly higher y-locations proceeding downstream. These locations correspond to where the W velocity profiles reach their maximum.

In this flow SSA lags behind FGA. The change in SSA from station to station is not as large as the FGA change. SSA gradually approaches FGA provided that there is no sudden change in FGA. Including station 3, FGA near the wall and in the outer layer increase in magnitude. At these stations near the wall below $y^+ = 20$ ($y/\delta \approx 0.009$), SSA values are close to FGA values. Above $y^+ = 100$ ($y/\delta \approx 0.04$) the change in SSA does not reflect the changes in FGA, although the change is in the same direction. Further downstream, FGA near the wall decreases in magnitude. The FGA profiles show a peak value of −25° at stations 5, 6 and 7. In the region away from the wall the

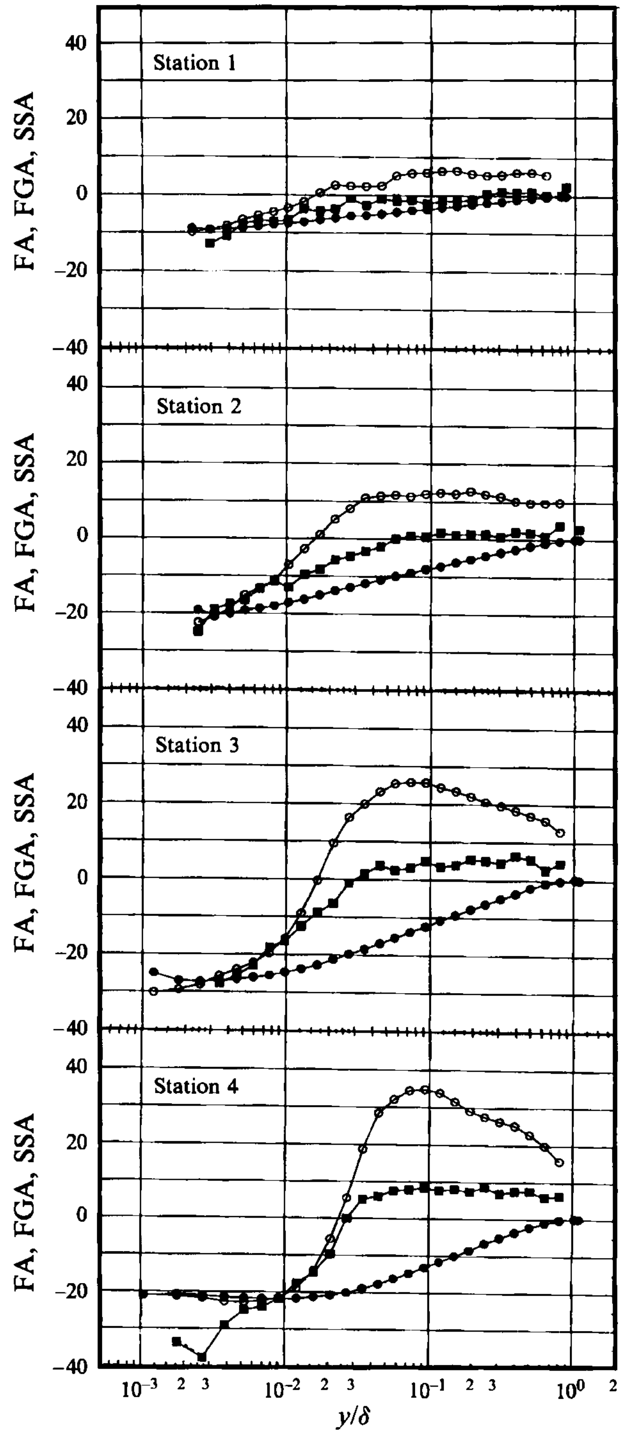

FIGURE 7. For caption see facing page.

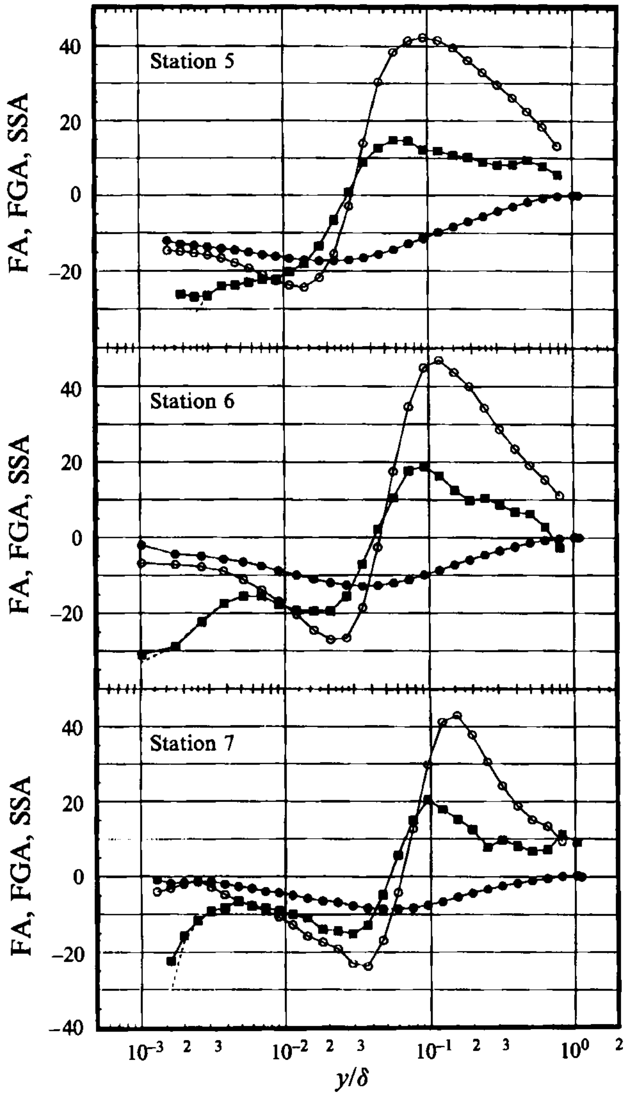

FIGURE 7. Flow angle, flow gradient angle, and shear stress angle computed using LDV data in free-stream coordinates for stations 1–7: ●, flow angle (FA); ○, flow gradient angle (FGA); ■, shear-stress angle (SSA). Dashed lines denote gradient-broadening-corrected SSA data. The uncertainties are on the order of the symbol size.

peak value increases till station 6; station 7 peak has a smaller value than that at station 6. At station 4 and at downstream stations SSA lags behind FGA in all regions of the layers. At station 1–4, above $y^+ = 100$ ($y/\delta \approx 0.04$) SSA is nearly a constant till the layer edge. At stations 5, 6 and 7 between $y^+ = 20$ and 200 ($y/\delta \approx 0.007$ and 0.07), FGA and SSA profiles intersect at two points. At all stations FA and FGA are close to each other near the wall below $y^+ = 10$. In a collateral flow region where FA is constant, FGA equals FA by definition. The FA changes all the way to the wall, especially at stations 5 and 6.

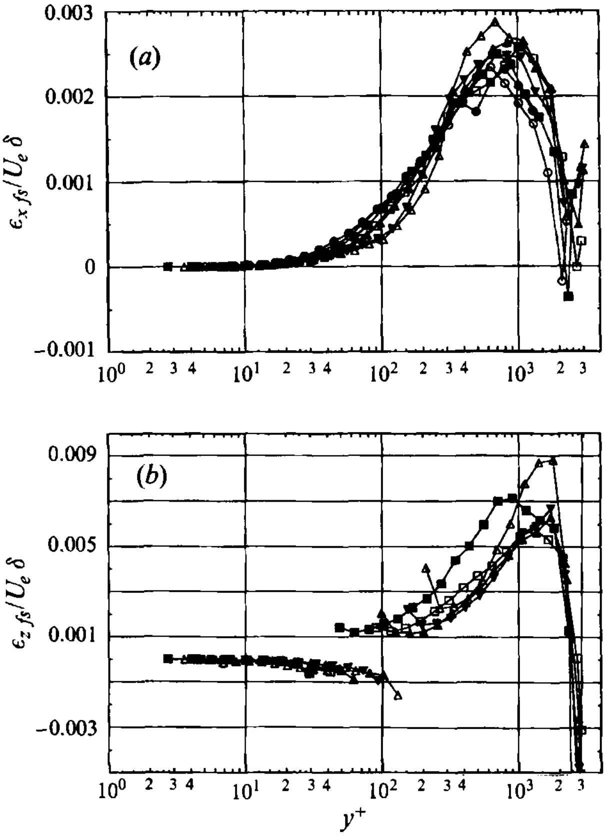

FIGURE 8. (*a*) *x* eddy viscosity $\epsilon_x/U_e\delta$ computed using the LDV data in free-stream coordinates. Stations: ●, 1; ○, 2; ■, 3; □, 4; ▲, 5; ▼, 6; △, 7. Typical uncertainty is $\pm 6\times 10^{-5}$. (*b*) As *a* but for *z* eddy viscosity $\epsilon_z/U_e\delta$. Typical uncertainty is $\pm 3\times 10^{-5}$.

5.2. *Eddy viscosities in the x- and z-directions*

The eddy viscosity in the local free-stream *x*-direction is computed using

$$\epsilon_{xfs} = \frac{-\overline{uv}}{\partial U/\partial y}$$

and shown non-dimensionalized with the local δ and U_e in figure 8(*a*). For all the stations, the profiles vary almost linearly near the wall, reach maxima of 0.0023 to 0.0028 in the $y^+ \approx 700$ to 1000 ($y/\delta \approx 0.25$ to 0.4) range, and decrease toward the free stream. Proceeding downstream, maxima in the profiles are reached with a steeper slope at a lower y^+ location.

The eddy viscosity in the *z*-direction of the FS coordinates is defined as

$$\epsilon_{zfs} = \frac{-\overline{vw}}{\partial W/\partial y}.$$

At stations 1 and 2, lateral-eddy-viscosity values are on the order of 0.01 to 0.02 due to small lateral velocity gradients and are omitted from the plot (figure 8*b*). Both the $-\overline{vw}$ stress and the lateral velocity gradients change sign at different y^+ locations in each profile. In the vicinity where the gradient value $\partial W/\partial y$ is zero, the values swing from $-\infty$ to $+\infty$. At these locations the symbols in figure 8(*b*) are not connected. The maximum value in each profile occurs within the $y^+ = 1000$ to 1500 ($y/\delta \approx 0.4$ to 0.6) region. The maximum at station 7 is approximately 0.009, which is about 3 times larger than the longitudinal eddy viscosity obtained from the same station.

5.3. *Anisotropy factor, N*

Many eddy-viscosity turbulence models of three-dimensional boundary layer flows assume that the shear stresses are related to the mean velocity gradients and that the eddy viscosity is isotropic and independent of the coordinate axes. The ratio of eddy viscosities in the transverse, ϵ_z- to the streamwise ϵ_x- axis directions in the (x, z)-plane defines the anisotropy factor N:

$$N = \frac{-\overline{vw}/(\partial W/\partial y)}{-\overline{uv}/(\partial U/\partial y)} = \frac{\tan(\mathrm{SSA})}{\tan(\mathrm{FGA})}$$

which is generally not unity and is coordinate-system dependent, according to data. In a coordinate system in which N is about constant, the shear stresses could be related to the mean flow variables using the eddy viscosity models and this anisotropy factor. With this consideration, N was plotted in three different coordinate systems.

Overall the N values are mostly less than 1 and sometimes negative, with no distinct form of variation in the profiles. The data in NS coordinates (figure 9*b*) are less scattered with respect to the data in the FS system (figure 9*a*); furthermore, data in WC coordinates (figure 9*c*) are in a narrower range than the data in NS coordinates. However, it should be noted that for different regions of the boundary layers at different stations, a different coordinate system may give a value closer to a constant. For example, above $y^+ \approx 350$ values in NS coordinates are closer to one another; near the wall WC coordinates produce more constant values. Near-wall values below $y^+ = 10$ attain very large positive numbers reaching well above 10 for many stations. Owing to the definition of the quantity at locations where the $\partial W/\partial y$ velocity gradient value tends towards zero, the numbers are large in magnitude, and these locations are shown with vertical lines in the figures.

In an attempt to generalize these observations and find the best *single* coordinate system with less scatter and less y variation for N, anisotropy factors in the three coordinate systems were calculated for the pressure-driven flow data of Anderson & Eaton (1987*b*, stations: S1, S2, S3, S4, S5), Dechow & Felsch (1977, stations: 1, 2, 3, 4, 5, 6, 7), Elsenaar & Boelsma (1974, stations: 1, 4, 5, 6, 7, 8, 9, 10), and Müller (1982, stations: B1, C2, D2, E3, F5). The average and the standard deviation of the values calculated in each coordinate system at several y^+ locations in the profiles are in table 6. These data show that isotropy in such a three-dimensional turbulent boundary layer is an exception, not the rule. The N anisotropy factor in wall-stress coordinates is more nearly constant with less scatter and less y variation.

From the physical viewpoint for practical calculations, the wall-stress coordinates are more closely aligned with the direction of the flow gradient in the region of the flow that has the largest stresses. In other words, the relatively large wall-region turbulent shear stresses control the flow more than the outer-layer stresses and should be more accurately modelled. The use of a constant N in wall-stress coordinates for the outer layer is certainly as good or better than a constant N in local free-stream coordinates.

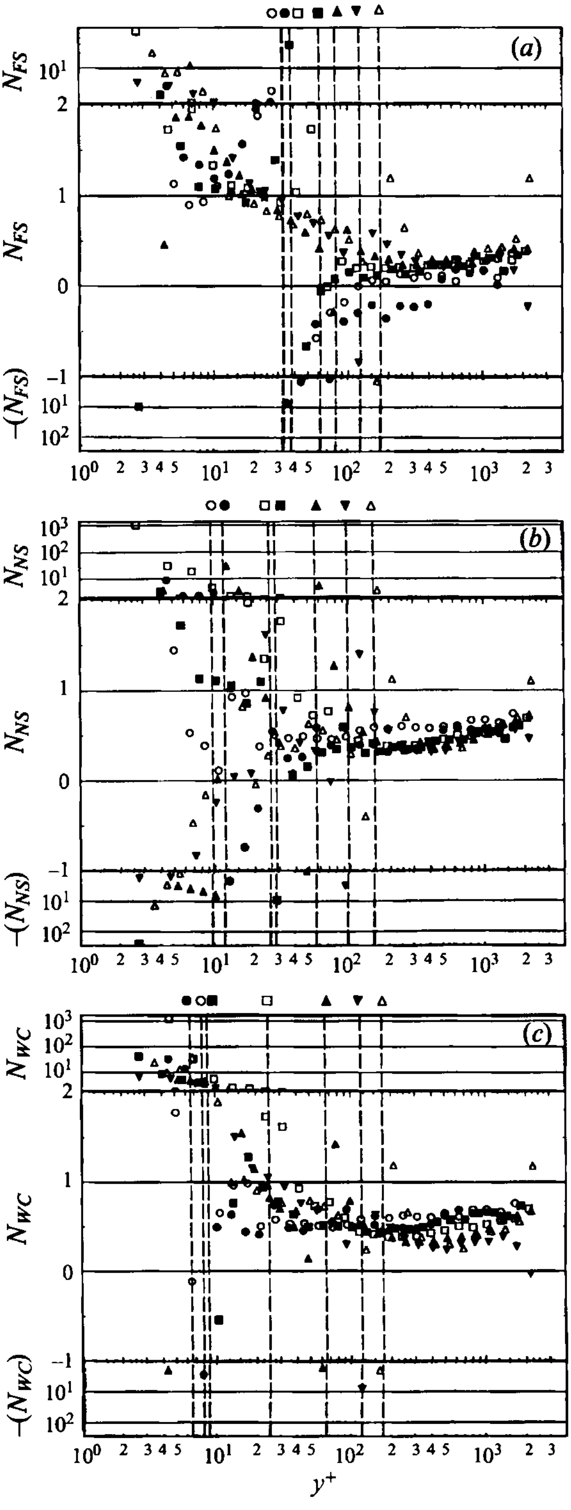

FIGURE 9. N, eddy viscosity anisotropy constant computed using LDV data in (*a*) free-stream coordinates, (*b*) normal-stress coordinates, and (*c*) wall-stress coordinates. Stations: ●, 1; ○, 2; ■, 3; □, 4; ▲, 5; ▼, 6; △, 7. Dashed vertical lines are for visual aid to note the locations where the flow gradient angle is 0. Typical uncertainty for N is ±0.06.

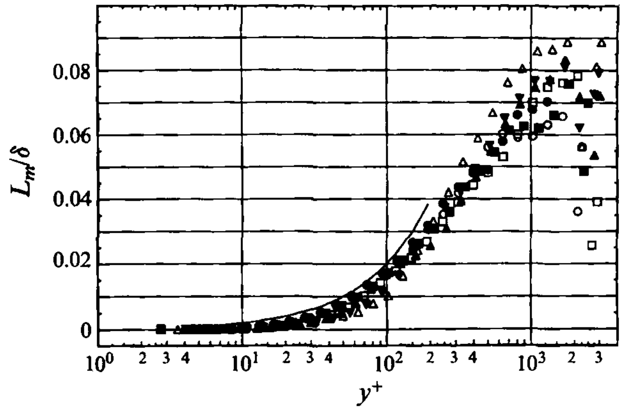

FIGURE 10. Mixing length non-dimensionalized with boundary layer thickness of each station separately computed using LDV data. Smooth curve denotes the $L_m/\delta = 0.41y/\delta$ for station 1. Stations: ●, 1; ○, 2; ■, 3; □, 4; ▲, 5; ▼, 6; △, 7. Typical uncertainty for L_m/δ is $\pm 8 \times 10^{-5}$.

	y^+	Average N	Standard deviation of N
Free-stream coordinates	70	0.933	5.86
	100	0.186	3.10
	250	−0.049	1.57
	500	0.272	1.19
	1000	0.574	0.67
Normal-stress coordinates	70	0.382	1.16
	100	0.193	1.65
	250	0.261	0.85
	500	0.503	0.764
	1000	0.663	0.541
Wall-stress coordinates	70	0.527	0.615
	100	0.274	1.52
	250	0.472	0.758
	500	0.596	0.593
	1000	0.649	0.537

TABLE 6. Average anisotropy and standard deviation calculated in different coordinate systems for Anderson & Eaton, Dechow & Felsch, Elsenaar & Boelsma, and Muller (pressure-driven flows)

5.4. *Mixing length*

The mixing length is computed using

$$L_m = \frac{(|\tau|/\rho)^{1/2}}{[(\partial U/\partial y)^2 + (\partial W/\partial y)^2]^{1/2}} = \frac{[(-\overline{uv})^2 + (-\overline{vw})^2]^{1/4}}{[(\partial U/\partial y)^2 + (\partial W/\partial y)^2]^{1/2}}$$

(Cebeci & Smith 1974) and presented in L_m/δ *vs.* y^+ coordinates (figure 10) which is independent of the coordinate system. These mixing length values are close to zero very near the wall below $y^+ \approx 20$, as is characteristic for the nearest wall region for two-dimensional flows. The model equation for the semi-logarithmic velocity profile region, $L_m/\delta = 0.41y/\delta$, is plotted for station 1 as a line. None of the station values follow the model equation: they either continuously increased to the layer edge or levelled at

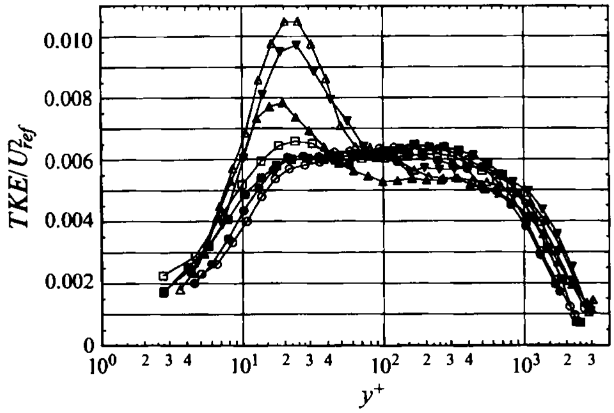

FIGURE 11. Turbulent kinetic energy profiles obtained using LDV data. Stations: ●, 1; ○, 2; ■, 3; □, 4; ▲, 5; ▼, 6; △, 7. Typical uncertainty for TKE/U^2_{ref} is $\pm 6 \times 10^{-5}$.

values different than 0.09, the approximate two-dimensional flow value (Townsend 1976). Experimental uncertainties in small measured values lead to more-scattered results near the outer edge.

5.5. *Turbulent kinetic energy*

The specific turbulent kinetic energy is

$$\text{TKE} = \tfrac{1}{2}(\overline{u^2}+\overline{v^2}+\overline{w^2})$$

and is non-dimensionalized with U^2_{ref} in figure 11. At the first three stations, the TKE of the flow is distributed similarly in the profiles. Starting with station 4, the large increase below $y^+ = 40$ for stations 4 and 5 and below $y^+ = 80$ for stations 6 and 7 is accompanied by a slight decrease for greater y^+. The increase in TKE at the last four stations near the wall is mainly due to increases in the $\overline{u^2}$ normal stress. All the profiles show a plateau region within $y^+ = 80$ to 300 where the TKE is nearly constant. Towards the wall and towards the free stream, the TKE monotonically approaches zero.

5.6. *Townsend's structural parameter*

Townsend's structural parameter A_1 is a measure of the correlation between the magnitude of the kinematic shear stress and turbulent kinetic energy:

$$A_1 = \frac{[(\overline{vw})^2+(\overline{uv})^2]^{1/2}}{\overline{u^2}+\overline{v^2}+\overline{w^2}} = \frac{|\tau/\rho|}{\overline{u^2}+\overline{v^2}+\overline{w^2}}$$

as shown in figure 12. The magnitude of the shear stress parallel to the wall $|\tau/\rho|$ and the turbulent kinetic energy do not change with coordinate system rotation about the y-axis. For two-dimensional flows $A_1 \approx 0.15 = -\overline{uv}/(2\ \text{TKE})$ in the middle of the boundary layer (Bradshaw, Ferris & Atwell 1967). With a similar relation in a three-dimensional TBL, the magnitude of the stress in a plane parallel to the wall could be related to the TKE. Thus, the TKE transport equation could be used to represent the transport of the magnitude of the shear stress.

At all stations values are less than 0.15. Below $y^+ = 15$ all station values are a

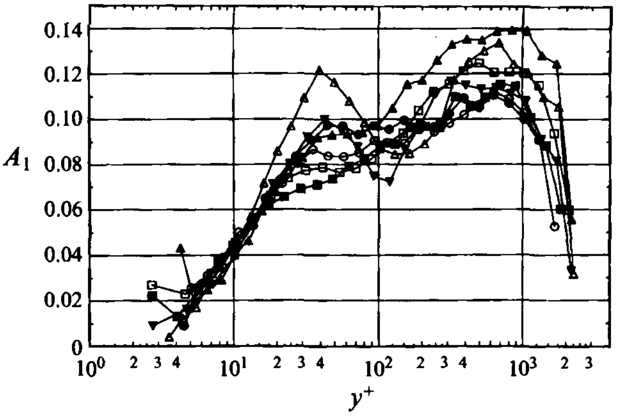

FIGURE 12. A_1, Townsend's structural parameter computed using LDV data. Stations: ●, 1; ○, 2; ■, 3; □, 4; ▲, 5; ▼, 6; △, 7. Typical uncertainty for A_1 is ± 0.006.

function of y^+. Nearest the wall $A_1 \sim y$ since the continuity equation requires that very near the wall $u \sim y$, $v \sim y^2$ and $w \sim y$. At station 1, above $y^+ = 40$ the values show a plateau within a range 0.09 to 0.11. At the next three stations within the $y^+ = 20$ to 200 range there is a decrease. Above this height the values are closer to those at station 1 with slightly increased values at station 4 and as much as 0.03 higher at station 5. Between $y^+ = 20$ and 40 at station 5, 6 and 7 there is an increase above the station 1 values. At stations 6 and 7 this increase is accompanied by a decrease at $y^+ = 150$. While station 6 values in the outer layer are on the order of station 1 values, at station 7 there is another increase resulting in values above those of station 4. These variations at different heights in the layers result in double-peaked A_1 profiles for station 6 and 7.

5.7. *Ratio of $\overline{v^2}$ normal stress to the stress magnitude*

The ratio $\overline{v^2}/|\tau/\rho|$, which is the ratio of the y-direction normal stress to the shear stress magnitude, is a correlation between the momentum-transporting velocity scale and the resulting magnitude of the shear stress and does not change with coordinate system rotation about the y-axis. From observation of near-wall two-dimensional mean flow data (Rotta 1962), it appears that $-\overline{uv}$ is proportional to $\overline{v^2}$. If a strong correlation exists for three-dimensional flows, it will provide a relationship such that given one value, the second may be calculated, thus reducing the number of simultaneous equations to be solved. Also, this velocity scale could be used in attempts to relate the shear stresses to the mean flow variables in a transport model.

Figure 13(*a*) shows $\overline{v^2}/|\tau/\rho|$ *vs.* y^+ outside the viscous sublayer and $|\tau/\rho|/\overline{v^2}$ *vs.* y/δ near the free stream for the present data together with the Klebanoff (1955) two-dimensional turbulent boundary layer data and Laufer (1954) pipe flow data. At the wall $\overline{v^2}/|\tau/\rho|$ must be zero and must vary linearly with y to satisfy the fluctuating mass continuity equation (Rotta 1962). Above $y^+ = 100$, this ratio is about constant for a given station with values around 2 until the outer region of the boundary layer. between $y^+ = 20$ and 100 the quantity varies semi-logarithmically. Below $y^+ = 20$ there is a reduction till $y^+ = 10$. However, below $y^+ = 10$ values increase once more. The linear variation required by the fluctuating continuity equation is not observed at these y^+ locations. This may be due to the lack of data nearer the wall. Near the free stream,

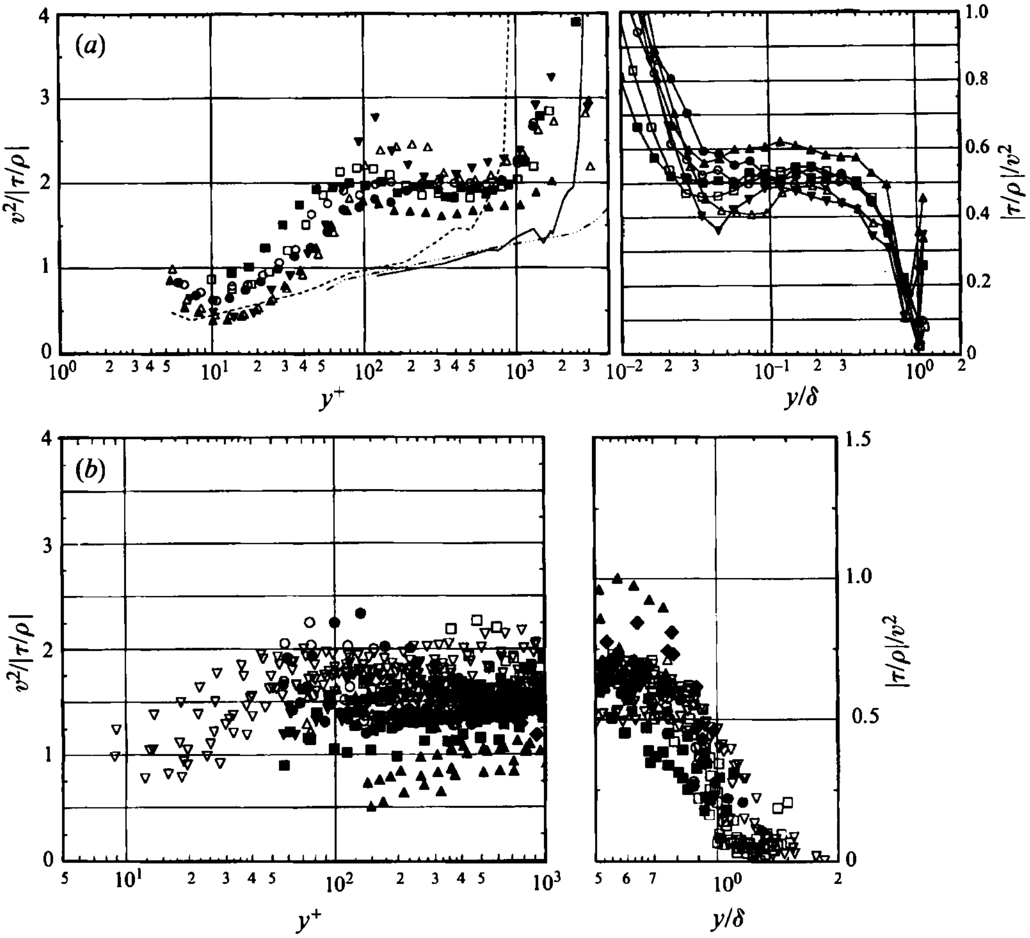

FIGURE 13. Ratio of $\overline{v^2}$ to the turbulent kinematic shear stress magnitude $|\tau/\rho|$ and the inverse ratio. (*a*) Computed using present LDV data: stations: ●, 1; ○, 2; ■, 3; □, 4; ▲, 5; ▼, 6; △, 7; ----, Klebanoff (1955); ——, Laufer (1954) (*Re* = 50000); ·····—····· Laufer (1954) (*Re* = 500000). Typical uncertainty both for $\overline{v^2}/|\tau/\rho|$ and $|\tau/\rho|/\overline{v^2}$ is ± 0.06. (*b*) Computed using other three-dimensional flow data: ●, Anderson & Eaton (S1, S2, S3, S4) (1987); ○, Dechow & Felsch (3, 4, 5, 6, 7) (1977); ■, Müller (B1, C2, D2, E3, F5) (1982); □, Elsenaar & Boelsma (4, 5, 6, 7, 8, 9, 10) (1974); ▲, Lohmann (2, 4, 9) (1976); ▼, Bissonnette & Mellor, low *Re* (5, 6, 7, 8) (1974); △, Bissonnette & Mellor, high *Re* (5, 6, 7, 8), (1974); ▽, Driver & Johnston (6, 7, 8, 9, 10, 11, 12) (1990); ◆, Littell & Eaton (radius = 0.421 case) (1991).

the $|\tau/\rho|/\overline{v^2}$ ratio should approach zero since irrotational free-stream fluctuations produce no shear stress. The increase in the quantity at the last two points of the profiles is due to uncertainty in the measured quantities. These results indicate that the Reynolds shear stress in a three-dimensional flow is lower relative to $\overline{v^2}$ than in a two-dimensional flow. There is less correlation between the *u*- and *v*- fluctuations.

The same conclusions can also be drawn from figure 13(*b*) for some other data sets. The stations where the flow is three-dimensional are given with the same notation as the original authors. For $y^+ > 50$ and $y/\delta < 0.5$, $\overline{v^2}/|\tau/\rho|$ values are almost a constant with an average value of 1.6; $|\tau/\rho|/\overline{v^2}$ reduces to zero near the layer edge.

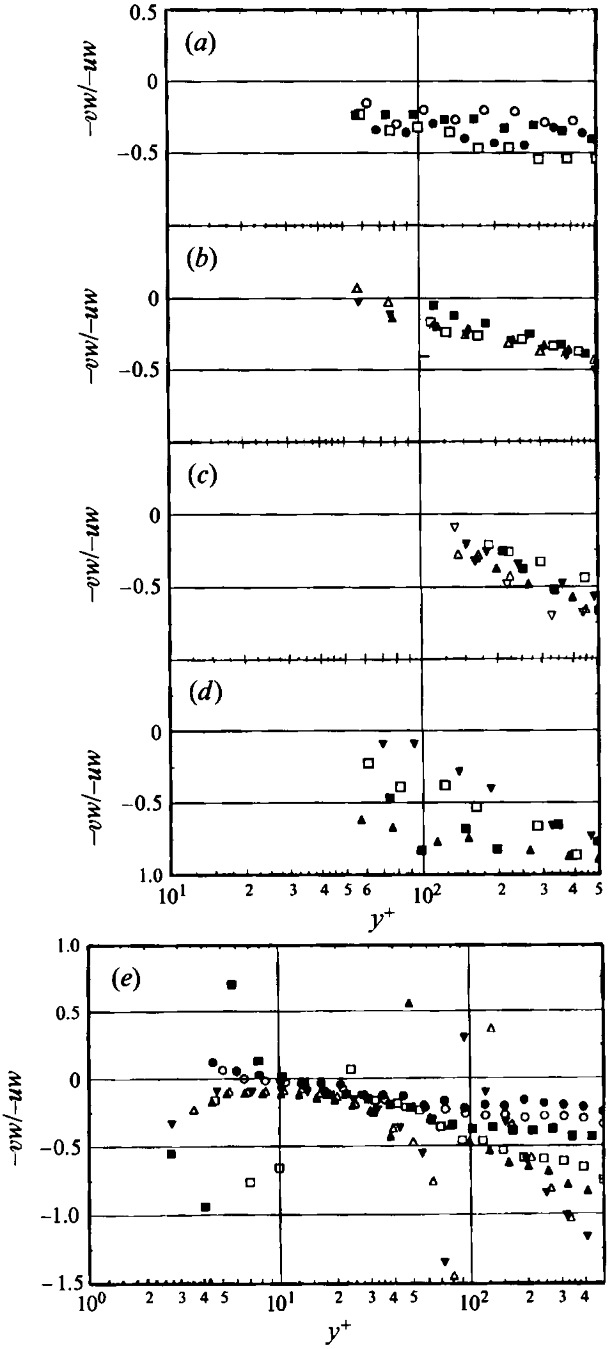

FIGURE 14. Ratio of $-\overline{vw}$ kinematic stress to $-\overline{vw}$ kinematic stress calculated in wall-stress coordinates. (*a*) Anderson & Eaton (●, S1; ○, S2; ■, S3; □, S4) (1987); (*b*) Dechow & Felsch (■, 3; □, 4; ▲, 5; ▼, 6; △, 7) (1977); (*c*) Elsenaar & Boelsma (■, 4; □, 5; ▲, 6; ▼, 7; △, 8; ▽, 9) (1974); (*d*) Müller (■, C2; □, D2; ▲, E3; ▼, F5) (1982); (*e*) present data (●, 1; ○, 2; ■, 3; □, 4; ▲, 5; ▼, 6; △, 7). Typical uncertainty for $-\overline{vw}/-\overline{uw}$ for the present flow is ±0.09.

5.8. *The ratio of two stresses,* $-\overline{vw}/-\overline{uw}$

The present data in the local free-stream coordinates show that the magnitude of $-\overline{uw}$ stresses is as high as or higher than the $-\overline{uv}$ shear stress magnitude at some stations and are higher than the $-\overline{vw}$ stresses. In wall-stress coordinates, these two stresses appear closely related. The ratio $-\overline{vw}/-\overline{uw}$ for the pressure-driven flows varies semi-logarithmically and correlates with y^+ near the wall up to $y^+ = 500$ (figure 14). For greater y^+, this ratio does not correlate well with y^+. The slope of the semi-logarithmic region is observed to change for different flows, but in each different flow it is about constant. This quantity shows that the v fluctuating velocity is less correlated with the w fluctuating velocity than the u fluctuating velocity as the wall is approached. Owing to the behaviour of the fluctuation continuity equation nearest the wall, this ratio must vary linearly with y and equal zero at the wall. The value of the ratio is subject to change in different coordinate systems.

6. Discussion

The three-dimensionality of the flow reported here is produced by the presence of the wing, which sets up pressure gradients across the test wall. Here we discuss these results in local free-stream coordinates. The $-\overline{uw}$ and $-\overline{vw}$ stresses are close to zero at station 1 since there is not yet a preferred correlation of the w fluctuating velocity with other fluctuations in the initial stages of the three-dimensional flow. The Reynolds-averaged Navier–Stokes equations with the boundary-layer approximations result in a set of equations in which $-\overline{uv}$ and $-\overline{vw}$ are the only important shear stresses. Thus, terms with the $-\overline{uw}$ shear stress are usually neglected as higher-order terms. However, the comparison of stresses at every station shows that $-\overline{uw}$ can be twice as large as $-\overline{uv}$.

At all stations the semi-logarithmic regions for the U mean velocity component are clearly visible. The W-component profiles show semi-logarithmically varying regions in a shorter range. The semi-logarithmic region seems to become shorter, which suggests that the overlap of inner-region and outer-region scalings progressively becomes less valid in this three-dimensional flow. A study (Ölçmen & Simpson 1992) of the near-wall similarity of three-dimensional flows using nine different data sets, including data for this flow, and nine different similarity relations showed that Johnston's (1960) similarity relation for the streamwise component of the velocity works best, even though none of the proposed relations shows a well-established law-of-the-wall velocity profile as observed in two-dimensional boundary layer flows.

The near-wall flow is most affected by the pressure gradients since the momentum of the fluid is lowest. By definition of the local free-stream coordinate system, the W mean velocity component at the layer outer edge is zero, as is the value at the wall, therefore $\partial W/\partial y$ at some point in the layer is zero. Proceeding downstream, the W velocity gradient changes its sign at a point in the layer progressively further away from the wall.

In a number of three-dimensional flows re-investigated as part of this study, the three-dimensionality of the flows is caused by lateral pressure gradients in a single direction. This results in the near-wall flow being more skewed from the undisturbed flow direction. For the present data the transverse pressure gradient changes sign, which makes the flow unique among these other flows. The effect of the sign change of the transverse pressure gradient is to decrease the wall-stress angle and the W mean velocity relative to the local free-stream direction. The near-wall normal stress $\overline{u^2}$ increases and $-\overline{vw}$ and $-\overline{uw}$ change sign.

The response of the shear stresses to the changes in pressure gradients is not well understood. Clearly though, the shear-stress angle lags behind the flow-gradient angle throughout the boundary layer, which shows that the stresses are not aligned with the rates of strain as in an isotropic continuum. Moin *et al.* (1990) show similar features from a direct numerical simulation of a low Reynolds number three-dimensional flow. Even in the viscous sublayer they show that SSA lags FGA by about 20°. An observation here is that the turbulence structure and preferred direction in the semi-logarithmic mean-velocity-profile region appears to be imposed on the sublayer turbulence. The coherency and correlation results of Ha & Simpson (1993) appear to support this idea.

Since the flow angle changes throughout the layers, different parts of the layers develop in different ways, i.e. different parts of the layer experience different history effects. The $\overline{u^2}$ normal stress data show that near the wall the stress increases, but away from the wall it decreases with increased three-dimensionality.

All of the flows discussed here show anisotropic eddy viscosities, which implies a difference between the rate-of-strain and shear-stress directions. Evaluation of four algebraic eddy-viscosity models from eight different three-dimensional data sets, including the present one, showed that the Johnson–King model worked best (Ölçmen & Simpson 1993). Another way of observing this lag is by showing the degree of anisotropy or how the eddy viscosities along different axes of a coordinate system differ. However, if N were a constant in a prescribed coordinate system, then the anisotropy of the flow or the eddy viscosities could be prescribed without needing to know the mechanism that produces it.

For any three-dimensional boundary layer flow, the flow gradient angle at the wall must be the same as the wall stress angle. Also, the flow angle very near the wall cannot be far from this value. Flow in the wall-stress coordinate system is observed to be more organized. In the wall-stress coordinate system, near the wall $-\overline{uv}$ is much larger than $-\overline{vw}$ since the x-axis of this coordinate system is in the direction of the wall shear stress and the turbulent stress direction is not grossly different from this value. Therefore, in these coordinates $-\overline{vw}$ is small in the viscous sublayer and develops further in the layer. The N anisotropy factor has less scatter than N calculated in local free-stream and normal-stress coordinate systems. The ratio of the two stresses $-\overline{vw}/-\overline{uw}$ seems to vary semi-logarithmically with y^+.

Another interesting observation in this coordinate system is that the ratio of the rate of production of $-\overline{vw}$ to the rate of production of $-\overline{uw}$ is nearly a constant over a range of y for a given station. The general form of production of $-\overline{u_i u_j}$ shear stress is written as (Townsend 1976)

$$-\left(\overline{u_i u_l}\frac{\partial U_j}{\partial x_l}+\overline{u_j u_i}\frac{\partial U_i}{\partial x_l}\right)$$

in which the tensor summation convention applies. After neglecting the derivatives with respect to x and z and assuming $|\overline{v^2}\,\partial W/\partial y| \gg |\overline{vw}\,\partial V/\partial y|$, the ratio of the production of these stresses can be written as

$$C=\frac{-\overline{vw}_{prod}}{-\overline{vw}_{prod}}=\frac{-(\overline{v^2}\,\partial W/\partial y)}{-\overline{uv}\,\partial W/\partial y+\overline{vw}\,\partial U/\partial y)}=\frac{\overline{v^2}\tan(\mathrm{FGA})}{\overline{uv}\tan(\mathrm{FGA})+\overline{vw}}.$$

For two-dimensional flows this ratio reduces to

$$C_{2D}=\frac{-\overline{v^2}}{-\overline{uv}}=-\frac{\overline{v^2}}{|\tau/\rho|}$$

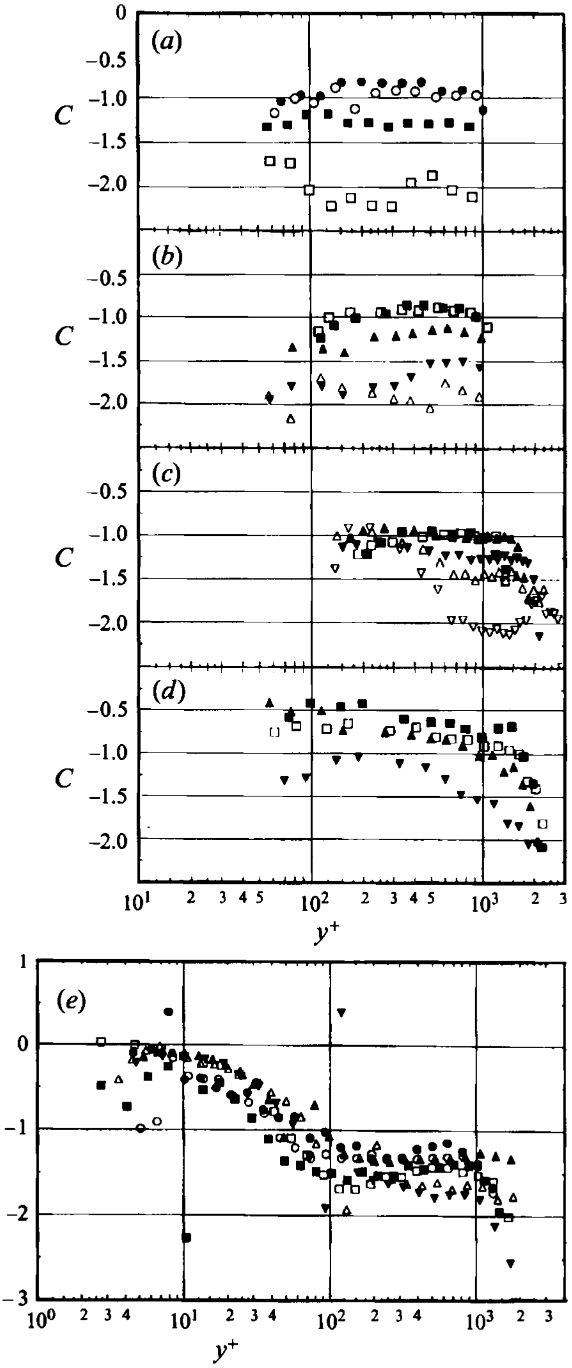

FIGURE 15. Ratio of the production of $\overline{vw}$ to the production of $\overline{uw}$ calculated in wall-stress coordinates. Symbols as in figure 14. Typical uncertainty for C for the present flow is ± 0.06.

which was observed in figure 13(*a*) to be close to -1. In three-dimensional flows the parameter gives a relation between the variation of several stresses. The C calculated for different flows are shown in figure 15. The C parameter changes from station to station, but it is close to a constant at each station over a range of y^+ from 100 to 1000, as observed in figures 13(*a*) and 13 (*b*) for $\overline{v^2}/|\tau/\rho|$. Figure 15 shows that even for downstream stations which show significant mean three-dimensional effects, C is nearly a constant as for two-dimensional flows.

The parameters N, $\overline{v^2}/|\tau/\rho|$, and C appear to be almost constant for $y^+ > 50$ and $y/\delta < 0.6$, as a first approximation. The assumption that any of the two parameters are constants even for one data station necessitates that the third parameter be a variable. The representative values for N and $\overline{v^2}/|\tau/\rho|$ were obtained after averaging many values. Therefore, for a specific location or for an entire station the values may be vastly different from the average values.

The ratios between other stress production terms can be written as

$$\frac{-\overline{vw}_{prod}}{-\overline{uv}_{prod}} = \tan(\mathrm{FGA}), \quad \frac{-\overline{uw}_{prod}}{-\overline{uv}_{prod}} = \frac{-\overline{uv}\tan(\mathrm{FGA}) - \overline{vw}}{-\overline{v^2}}$$

with the assumption that $|\overline{v^2}\,\partial U/\partial y| \gg |\overline{uv}\,\partial V/\partial y|$. Using these relations N may be reexpressed as

$$N = \frac{-\overline{uv}_{prod}/-\overline{uv}}{-\overline{vw}_{prod}/-\overline{vw}}.$$

Thus, another interpretation for N is possible. It is the ratio of production of the stress normalized with the value of the major stress of interest. If N is less than 1 it shows that production of $-\overline{uv}$ with respect to $-\overline{uv}$ is less than production of $-\overline{vw}$ with respect to the value of $-\overline{vw}$.

7. Conclusions

A high Reynolds number three-dimensional turbulent boundary layer generated by a 3:2 elliptical-nose NACA 0020 tail cylinder protruding from a flat plate was studied experimentally using a three-velocity-component LDV capable of examining the viscous sublayer for $y^+ > 3$. The data were used to investigate the mean flow and Reynolds stresses characteristics.

The anisotropy constant N, which is the ratio of the eddy viscosities in the z- and x-directions, is not unity as is frequently used in turbulence closure models. Although in local wall-stress coordinates, N_{WC} is close to 0.6, it varies through the boundary layer and from station to station. Thus, the concept of isotropy or even the constancy of the ratio N in a preferred direction is questionable. While the mixing lengths computed from the data near the wall crudely follow $0.41y$, they have different levels in the outer region of each measurement station.

The comparison of shear stress and flow-gradient angles revealed that the shear-stress angle lags behind the flow-gradient angle, especially in the inner region. In the outer region, the lag was more distinguishable at the downstream stations. The anisotropy of the near-wall turbulence is greater than in the outer regions.

The TKE profiles show that at successive locations the TKE of the flow increases near the wall but decreases away from the wall. The structural parameter A_1, relating the shear stresses to the TKE of the flow, is lower than 0.15 in the outer region, and substantially less than 0.15 near the wall, with double peaks at some stations.

The $\overline{v^2}/|\tau/\rho|$ results from these and other data sets show that at stations where the three-dimensional effects are largest, the ratio is higher than obtained for two-dimensional flows, which is due to less correlation between the u- and v-velocity fluctuation components. The ratio is approximately constant between $y^+ = 100$ and 1000, with a value of 1.6.

The ratio $-\overline{vw}/-\overline{uw}$ in the wall-stress coordinates varies semi-logarithmically for three-dimensional flow stations of many pressure-driven flows, which gives a relation to be used in modelling Reynolds stress transport equations. Another interesting relation is that for many stations of several pressure-driven flows, the ratio C (production of $-\overline{vw}$/production of $-\overline{uw}$) is a constant within a range of y at a given station, but changes from station to station.

The authors gratefully acknowledge the support of the Office of Naval Research and the Defense Advanced Research Projects Agency under Grants N00014-89-J-1275 and N00014-90-J-1909.

REFERENCES

AHN, S. 1986 Unsteady features of turbulent bounday layers. MS thesis, Dept. of Aerospace and Ocean Engng, VPI&SU.

AILINGER, K. 1990 Measurements of surface shear stresses under a three-dimensional turbulent boundary layer using oil-film interferometry. MS thesis, Dept. of Aerospace and Ocean Engng, VPI&SU, Report VPI-AOE-173; circulated by DTIC.

ANDERSON, S. D. & EATON, J. K. 1987*a* An experimental investigation of pressure-driven three-dimensional turbulent boundary layers. *Rep.* MD-49. Thermosciences Div., Dept of Mechanical Engrg, Stanford University.

ANDERSON, S. D. & EATON, J. K. 1987*b* Experimental study of a pressure-driven three-dimensional turbulent boundary layer. *AIAA J.* **25**, 1086–1092.

BERG, B. VAN DEN 1987 Three-dimensional shear layer experiments and their use as test cases for calculation methods. *AGARD-Rep.* 741.

BERTIN, J. J. & SMITH, M. L. 1979 *Aerodynamics for Engineers*, First Edn, pp. 63–68. Prentice Hall.

BISSONNETTE, L. R. & MELLOR, G. L. 1974 Experiments on the behaviour of an axisymmetric turbulent boundary layer with a sudden circumferential strain. *J. Fluid Mech.* **63**, 369–413.

BRADSHAW, P. 1987 Physics and modelling of three-dimensional boundary layers. *AGARD Rep.* 741.

BRADSHAW, P., FERRISS, D. H. & ATWELL, N. P. 1967 Calculation of boundary layer development using the energy equation. *J. Fluid Mech.* **28**, 593–616.

CEBECI, T. & SMITH, A. M. O. 1974 *Analysis of Turbulent Boundary Layers.* Academic.

DECHOW, R. & FELSCH, K. O. 1977 Measurements of the mean velocity and of the Reynolds stress tensor in a three-dimensional turbulent boundary layer induced by a cylinder standing on a flat wall. *Symposium on Turbulent Shear Flows*, pp. 9.11–9.20 April 18–20, University Park, PA.

DEVONPORT, W. J. & SIMPSON, R. L. 1986 Some time-dependent features of turbulent appendage-body juncture flows. *16th Symp. on Naval Hydrodynamics, July 14–18, Berkeley, CA.*

DEVENPORT, W. J. & SIMPSON, R. L. 1990*a* Time-dependent and time-averaged turbulence structure near the nose of a wing–body junction. *J. Fluid Mech.* **210**, 23–55.

DEVENPORT, W. J. & SIMPSON, R. L. 1990*b* An experimental investigation of the flow past an idealized wing-body junction: *Final report.* Dept. of Aerospace and Ocean Engng, VPI&SU, Report VPI-AOE-172, circulated by DTIC.

DEVENPORT, W. J. & SIMPSON, R. L. 1992 Flow past a wing-body junction – experimental evaluation of turbulence models. *AIAA J.* **30**, 873–881.

DICKINSON, S. C. 1986 An experimental investigation of appendage-flat plate junction flow, volume I: description. DTNSRDC-886/051. David W. Taylor Naval Ship Research and Development Center.

DRIVER, D. M. & JOHNSTON, J. P. 1990 Experimental study of a three-dimensional shear-driven turbulent boundary layer with streamwise adverse pressure gradient. *Rep.* MD-57. Thermosciences Div. Dept of Mechanical Engng, Stanford University.

ECHOLS, W. H. & YOUNG, J. W. 1963 Studies of portable air-operated aerosol generators. *NRL Rep.* 5929.

ELSENAAR, A. & BOELSMA, S. H. 1974 Measurements of the Reynolds stress tensor in a three-dimensional turbulent boundary layer under infinite swept wing conditions. *NLR TR* 74095 21.

FERNHOLZ, H. H. & VAGT, J. D. 1981 Turbulence measurements in an adverse-pressure gradient three-dimensional turbulent boundary layer along a circular cylinder. *J. Fluid Mech.* **111**, 233–269.

FLEMING, J. L., SIMPSON, R. L. & DEVENPORT, W. J. 1993 An experimental study of a turbulent wing-body junction and wake flow. *Exps. Fluids* **14**, 366–378.

FREDERICK, D. & CHANG, T. S. 1972 *Continuum Mechanics*, p. 11. Cambridge: Scientific Publishers, Inc.

FUCHS, W., NOBACH, H. & TROPEA, C. 1994 Laser Doppler anemometry data simulation: application to investigate the accuracy of statistical estimators. *AIAA J.* **32**, 1883–1889.

GEORGE, W. K. & LUMLEY, J. L. 1973 The laser-Doppler velocimeter and its application to the measurement of turbulence. *J. Fluid Mech.* **60**, 321–362.

HA, S. M. & SIMPSON, R. L. 1993 An experimental study of coherent structures in a three-dimensional turbulent boundary layer. *VPI&SU Rep.* VPI-AOE-205, August 15, 1993; submitted to DTIC; manuscript submitted to *J. Fluid Mech.*

HEPNER, T. E. 1994 State-of-the-art laser Doppler velocimeter signal processors: calibration and evaluation, *AIAA Paper*, 94-0042.

JOHNSTON, J. P. 1960 On the three-dimensional turbulent boundary layer generated by secondary flow. *Trans ASME* D: *J. Basic Engng* **56**, 233–248.

JOHNSTON, J. P. 1976 Experimental studies in three dimensional turbulent boundary layers. *Rep.* MD-34, Thermosciences Div., Dept. of Mechanical Engineering, Stanford University.

JORGENSEN, F. E. 1971 Directional sensitivity of wire and fiber-film probes, an experimental study. *DISA Information*, no. 11, pp. 31–37.

KLEBANOFF, P. S. 1955 Characteristics of turbulence in a boundary layer with zero pressure gradient. *NACA Rep.* 1247.

LAUFER, J. 1954 The structure of turbulence in fully developed pipe flow. *NACA Rep.* 1174.

LIGRANI, P. M. & BRADSHAW, P. 1987 Spatial resolution and measurement of turbulence in the viscous sublayer using subminiature hot-wire probes. *Exps Fluids* **5**, 407–417.

LITTELL, H. S. & EATON, J. K. 1991 An experimental investigation of the three-dimensional boundary layer on a rotating disk. *Rep.* MD-60, Thermosciences Div., Dept of Mechanical Engng, Stanford University.

LOHMANN, R. P. 1976 The response of a developed turbulent boundary layer to local transverse surface motion. *Trans. ASME* I: *J. Fluids Engng* 354–363.

MCMAHON, H., HUBBART, J. & KUBENDRAN, L. 1982 Mean velocities and Reynolds stresses in a juncture flow. *NASA Contractor Rep.* 3605.

MERATI, P., MCMAHON, H. M. & YOO, K. M. 1988 Experimental modeling of a turbulent flow in the junction and wake of an appendage flat plate. *1st Natl Fluid Dynamics Congr., Cincinatti, OH.*

MILLER, J. A. 1976 A simple linearized hot-wire anemometer. *Trans. ASME* I: *J. Fluids Engng* **98**, 550–557.

MOIN, P., SHIH, T.-H., DRIVER, D. & MANSOUR, N. N. 1990 Direct numerical simulation of a three-dimensional turbulent boundary layer. *Phys. Fluids* A **2**, 1846–1853.

MONSON, D. J. 1984 A laser interferometer for measuring skin friction in three-dimensional flows. *AIAA J.* **22**, 557–559.

MONSON, D. J. & HIGUCHI, H. 1981 Skin friction measurements by a dual-laser-beam interferometer technique. *AIAA J.* **19**, 739–744.

MÜLLER, U. R. 1982 Measurement of the Reynolds stresses and the mean flow field in a three-dimensional pressure-driven boundary layer. *J. Fluid Mech.* **119**, 121–153.

ÖLÇMEN, M. S. 1990 An experimental study of a three-dimensional pressure-driven turbulent boundary layer. PhD dissertation, Aerospace and Ocean Engineering, Virginia Polytechnic Institute and State University.

ÖLÇMEN, M. S. & SIMPSON, R. L. 1992 Perspective: on the near wall similarity of three-dimensional turbulent boundary layers. *Trans. ASME* I: *J. Fluids Engng* **114**, 497–495.

ÖLÇMEN, M. S. & SIMPSON, R. L. 1993 Evaluation of algebraic eddy-viscosity models in 3-D turbulent boundary layer flows. *AIAA J.* **31**, 1545–1554.

ÖLÇMEN, M. S. & SIMPSON, R. L. 1994*a* A 5-velocity-component laser-Doppler velocimeter for measurements of a three-dimensional turbulent boundary layer. *Seventh Intl Symp. on Applications of Laser Techniques to Fluid Mechanics, 11–14 July 1994, Lisbon, Portugal* (*Measurement Sci. Tech.* to appear).

Ölçmen, M. S. & Simpson, R. L. 1994*b* A fiber-optic 5 component laser Doppler velocimeter. *NASA Contractor Rep.* to be completed.

Rotta, J. C. 1962 Turbulent boundary layers in incompressible flow. In *Progress in Aeronautical Sciences*, Vol. 2 (ed. A. Ferri, D. Küchemann & L. H. G. Sterne). Pergamon.

Schwarz, W. R. & Bradshaw, P. 1992 Three dimensional turbulent boundary layer in a 30 degree bend: experiment and modelling. *Rep.* MD-61. Thermosciences Div., Dept of Mechanical Engineering, Stanford University.

Shabaka, I. M. M. A. & Bradshaw, P. 1981 Turbulent flow measurements in an idealized wing-body junction. *AIAA J.* **19**, 131–132.

Simpson, R. L., Heizer, K. W. & Nasburg, R. E. 1979 Performance characteristics of a simple linearized hot-wire anemometer, *Trans. ASME* I: *J. Fluids Engng* **101**, 381–382.

Townsend, A. A. 1976 *The Structure of Turbulent Shear Flow*, 2nd Edn. Cambridge University Press.